Acta Biomaterialia 185 (2024) 281–295

Contents lists available at ScienceDirect

Acta Biomaterialia

journal homepage: www.elsevier.com/locate/actbio

Full length article

Quantitative atlas of collagen hydrogels reveals mesenchymal cancer cell traction adaptation to the matrix nanoarchitecture

Pablo Blázquez-Carmona[a,b,1], Raquel Ruiz-Mateos[a,b,1], Jorge Barrasa-Fano[c], Apeksha Shapeti[c], José Enrique Martín-Alfonso[d], Jaime Domínguez[a,b], Hans Van Oosterwyck[c], Esther Reina-Romo[a,b,2], José Antonio Sanz-Herrera[a,b,2,*]

[a] Escuela Técnica Superior de Ingeniería, Universidad de Sevilla. Avenida Camino de los Descubrimientos s/n, 41092 Sevilla, Spain
[b] Instituto de Biomedicina de Sevilla (IBIS). C. Antonio Maura Montaner, 41013 Sevilla, Spain
[c] Department of Mechanical Engineering, Biomechanics Section, KU Leuven, Celestijnenlaan 300. B-3001 Heverlee, Belgium
[d] Escuela Técnica Superior de Ingeniería, Universidad de Huelva. Avda. de las Fuerzas Armadas s/n, 21007 Huelva, Spain

ARTICLE INFO

Article history:
Received 26 February 2024
Revised 1 July 2024
Accepted 2 July 2024
Available online 9 July 2024

Keywords:
Mechanobiology
Breast cancer cells
Traction force microscopy
Tumor microenvironment
Cell morphology
FIB-SEM

ABSTRACT

Collagen-based hydrogels are commonly used in mechanobiology to mimic the extracellular matrix. A quantitative analysis of the influence of collagen concentration and properties on the structure and mechanics of the hydrogels is essential for tailored design adjustments for specific *in vitro* conditions. We combined focused ion beam scanning electron microscopy and rheology to provide a detailed quantitative atlas of the mechanical and nanoscale three-dimensional structural alterations that occur when manipulating different hydrogel's physicochemistry. Moreover, we study the effects of such alterations on the phenotype of breast cancer cells and their mechanical interactions with the extracellular matrix. Regardless of the microenvironment's pore size, porosity or mechanical properties, cancer cells are able to reach a stable mesenchymal-like morphology. Additionally, employing 3D traction force microscopy, a positive correlation between cellular tractions and ECM mechanics is observed up to a critical threshold, beyond which tractions plateau. This suggests that cancer cells in a stable mesenchymal state calibrate their mechanical interactions with the ECM to keep their migration and invasiveness capacities unaltered.

Statement of significance

The paper presents a thorough study on the mechanical microenvironment in breast cancer cells during their interaction with collagen based hydrogels of different compositions. The hydrogels' microstructure were obtained using state-of-the-art 3D microscopy, namely focused ion beam-scanning electron microscope (FIB-SEM). FIB-SEM was originally applied in this work to reconstruct complex fibered collagen microstructures within the nanometer range, to obtain key microarchitectural parameters. The mechanical microenvironment of cells was recovered using Traction Force Microscopy (TFM). The obtained results suggest that cells calibrate tractions such that they depend on mechanical, microstructural and physicochemical characteristics of the hydrogels, hence revealing a steric hindrance. We hypothesize that cancer cells studied in this paper tune their mechanical state to keep their migration and invasiveness capacities unaltered.

© 2024 The Author(s). Published by Elsevier Ltd on behalf of Acta Materialia Inc.
This is an open access article under the CC BY-NC-ND license
(http://creativecommons.org/licenses/by-nc-nd/4.0/)

1. Introduction

Cancer is a devastating disease with an increasing incidence worldwide. This incidence is estimated to rise to 40 % by 2040 [1]. Female breast cancer has surpassed lung cancer as the most diagnosed cancer, with an estimated 2.3 million new cases worldwide [1]. Current therapies and treatments remain challenging and

* Corresponding author at: Avenida Camino de los Descubrimientos s/n, 41092 Seville, Spain.
E-mail address: jsanz@us.es (J.A. Sanz-Herrera).
[1] These authors have contributed equally to this work.
[2] Joint senior authorship.

https://doi.org/10.1016/j.actbio.2024.07.002
1742-7061/© 2024 The Author(s). Published by Elsevier Ltd on behalf of Acta Materialia Inc. This is an open access article under the CC BY-NC-ND license (http://creativecommons.org/licenses/by-nc-nd/4.0/)

reflect incomplete understanding of the underlying biology of this ample disease. It occurs due to a genomic instability induced and regulated by external signals in the microtumoral environment, which leads to tumor development and evolution, this being a dynamic process of extraordinary multifactorial complexity.

In the past decades, there has been a significant recognition of the prominent role of the extracellular matrix (ECM) in cancer [2-4]. The ECM is a complex three-dimensional acellular assembly of macromolecules and interconnected cell-scale fibers [5]. It determines the apparent and local mechanical properties of a tissue providing a dynamic and bioactive structure that actively influences critical cell behaviors through mechanotransduction [5,6]. This multidirectional interaction impacts cell signaling pathways, influencing cellular behaviors such as growth, differentiation, apoptosis, migration, gene expression and signal transduction [2,7-11].

In general, cell spreading, and migration are significatively dependent on the ECM stiffness and viscoelasticity [12,13]. In 2D environments, cell spreading seems to be exclusively dominated by an increase in substrate stiffness. Stiffer ECM stabilizes adhesions while attachments have less stability and faster dynamics in softer substrates [14,15]. In 3D, cell spreading occurs in microporous matrices of sufficient stiffness [16]. Migration patterns vary mainly depending on the pore size of the ECM; larger pores allow robust migration [17,18], while smaller pores require degradation or mechanical forces to create migration channels [19]. Nevertheless, it is unclear to date whether the nanoarchitectural obstacles imposed by the size of the ECM open spaces and the dense three-dimensional microenvironment surrounding the tumor act as a barrier to metastasis at certain lower porosity bound. In line with this, recent studies suggest that highly invasive cancer cells can adapt their phenotype to the microenvironment to migrate through it, regardless of any potential barriers [20]. Solon et al. [21] also reported that 2D cellular morphology and internal stiffness, governed by the assembly of the cytoskeleton or the internal stress, is also regulated by the mechanical properties of the substrate. Furthermore, ECM stiffness and porosity affect cell apoptosis. Softer substrates in 2D cultures promote higher levels of apoptosis, while apoptosis can be triggered by confinement or restricted cell volume in 3D substrates [12]. Regarding long-timescale processes, including division and differentiation, the literature demonstrates that the response of cells to substrate stiffness and microstructure is highly cell-type specific, as well as dependent on the type of adhesion ligands to which the cell adheres [22]. In particular, the breast cancer cell line MDA-MB-231, proliferates rapidly as substrate stiffness increases [23].

The extracellular matrix also undergoes remodeling with cellular interactions. Cells respond to mechanical stimuli by altering the ECM, modifying crosslinks or secreting enzymes, thus leading to a change of behavior of adjacent cells [24,25]. In non-linear elastic matrices, the fibers align and increase the stiffness locally, promoting higher cell force generation [26]. However, this positive mechanical feedback loop between cells and ECM absents in linear elastic microenvironments [16]. Increased ECM density and stiffness is observed during cancer progression and has been linked with alterations in breast cancer cell metabolism [27,28]. For example, it has been shown that healthy breast tissue (with a Young's modulus of 0.2 kPa) is softer than a cancerous tissue (with a Young's modulus of 4 kPa) in advanced malignancy [29].

To understand the *in vivo* complexity and discover new approaches of cancer therapies, cell culture plays an important role, from drugs development to modelling of cell–ECM interactions. Traction force microscopy (TFM) is one of the most popular methodologies to quantify forces exerted by cells and to characterize their mechanical microenvironment. For this purpose, *in vitro* models of cellular systems are embedded in natural/artificial matrices. The mechanical activity of cells is then registered as follows: first, the displacement field is reconstructed in the hydrogel volume by using fiducial markers (e.g. fluorescent beads), from a cellular stressed state versus a relaxed one. Then, cellular tractions are computed at the boundary of the cell, provided the mechanical modeling and characterization of the matrix [30]. TFM has been applied both to 2D [31-34] as well as 3D *in vitro* systems [35-37], to cite a few. Using this methodology, the mechanical microenvironment of cancer cells has been investigated in several works. For instance, Peschetola et al. [38] correlated epithelial bladder cancer cell line stresses with cancer invasiveness. Rabinovitz et al. [39] used a traction-force detection assay to detect forces exerted by carcinoma cells through integrin $\alpha 6\beta 4$, demonstrating that this integrin can transmit forces without the need to engage other integrins. Figueiredo et al. [40] used micropattern traction force microscopy to elucidate the molecular machinery involved in the invasiveness of gastric cancer cells mediated by E-cadherin mutations. Additionally, other studies consider cancer cell lines in TFM experiments, just to evaluate the TFM methodology or as examples of applications of alternative formulations of TFM [41-43].

On the other hand, different cellular *in vitro* systems have been investigated under different compositions of the matrix hydrogel. Hydrogels with tunable mechanical properties have been massively used in different applications in the last years (see the Tse & Engler [44] and Li et al. [45] for a review, and references therein). Herrick et al. [46] synthesized poly(ethylene glycol) (PEG) and phosphorylcholine (PC) with different stiffnesses, to study how substrate mechanical properties influence cell morphology, focal adhesion structure, and proliferation; across multiple mammalian cell lines. On a step forward, Shayan et al. [47] developed controllable stress relaxation rate and stiffness hydrogels to modulate endothelial cell behavior. Liu et al. [48] also reported that liver carcinoma functional response can be modulated by tuning the nonlinear elastic response, i.e. strain stiffening region, of polyisocyanide hydrogels. Moreover, recent studies have pointed out how the use of stiff hydrogels can induce a mechanical memory into the tumor cells due to epigenetic modifications that enable them to retain the biophysical adaptations acquired in the primary microenvironment even after their transference to softer substrates [49]. A few studies have also attempted controlling hydrogels' microstructure [50-52] and microarchitectural organization [53,54].

Despite all this extensive research in this field, the impact of hydrogels' microarchitectural features, mechanical properties and hydrogels' source on tumor mechanical microenvironment have not been thoroughly investigated. This work aims to characterize and investigate the mechanical microenvironment of breast cancer cells as they interact with several different hydrogels. In particular, human MDA-MB-231 breast cancer cells were embedded in collagen I type hydrogels from different natural sources, and hence different physicochemical compositions. Hydrogels were mechanically tested in shear rheology assays, and their microarchitectures were also characterized using state-of-the-art 3D microscopy techniques, namely focused ion beam-scanning electron microscope (FIB-SEM). FIB-SEM was originally applied in this work to collagen matrices, and it allowed the reconstruction of complex fibered microstructures with extreme accuracy within the nanometer (nm) range, to obtain key microarchitectural parameters such as fiber density or pore size, amongst others. The state of the art for evaluating fibered matrix morphology in the context of cell mechanics is performed through optical methods that still provide incomplete and/or inaccurate structural information of the fiber network [55]. Cellular tractions, displacements and strain energies of breast cancer cells were measured using 3D TFM, as indicators of their mechanical microenvironment, for the different considered cases. The battery of collected results allowed us to explore the impact of mechanical, physicochemical and microarchitectural matrix features at

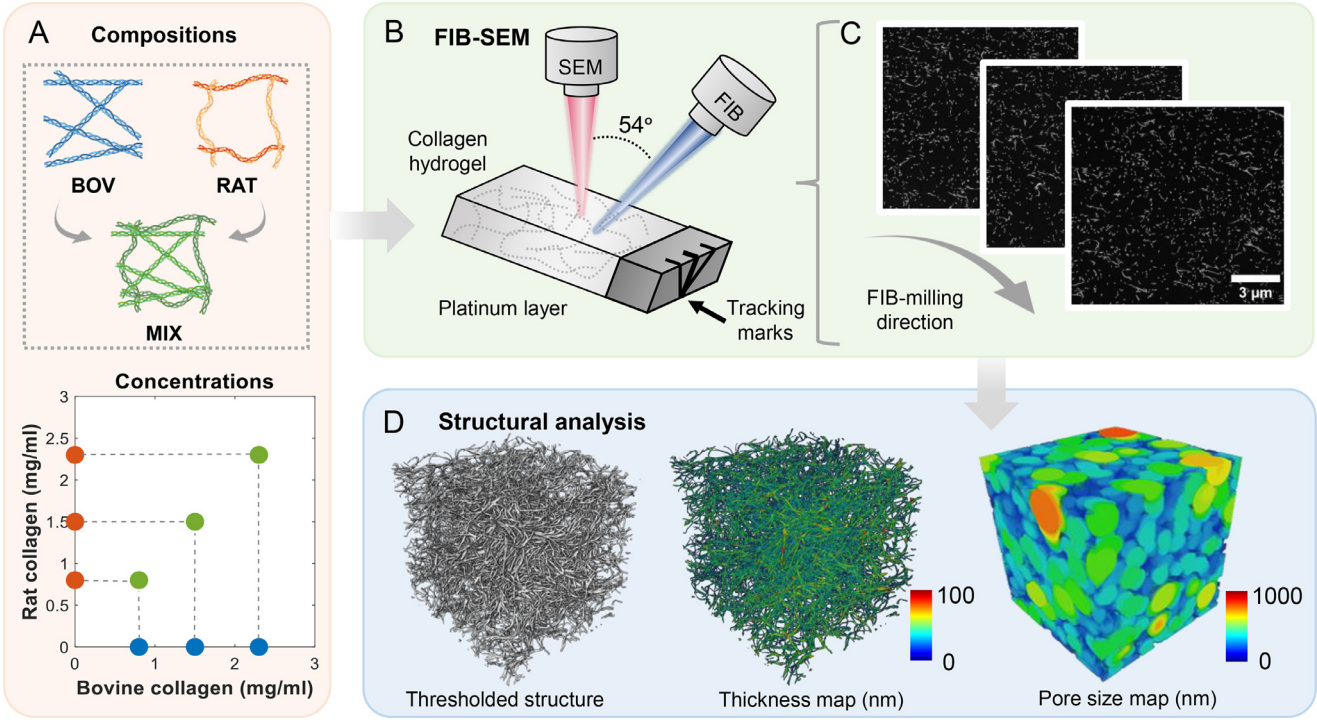

Scheme 1. Scheme of the prepared collagen-based hydrogels and overview of the FIB-SEM imaging procedure to characterize the microstructure of the hydrogels. A) Types of collagens as a base material for the hydrogels: bovine dermis-based (BOV), rat tail-based (RAT) and mixed collagen (MIX) and concentrations studied for each composition: 0.8, 1.5 and 2.3 mg/ml. B) Scheme of the FIB-SEM setup. The focused ion beam (FIB) and SEM (scanning electron microscope) columns are oriented at a 54-degree angle and positioned to coincide on the surface of the hydrogel at a single point. Tracking marks in a lateral platinum protective layer allow correcting misaligned sections in further post-processing. C) Examples of the hydrogel's surface scanned using FIB-SEM. D) 3D-reconstruction of the collagen structure after post-processing and thresholding the acquired images (6 × 6 × 6 µm) and its fiber thickness and pore size maps.

the nanometer scale on the micromechanical environment of tumoral cells.

2. Materials and methods

2.1. Collagen-based hydrogel preparation

Nine different type I collagen hydrogels were studied with collagen sourced from only bovine dermis (BOV), only rat tail (RAT), or a 1:1 combination of both (MIX); at concentrations of 0.8, 1.5, or 2.5 mg/ml, as illustrated in Scheme 1A. Bovine dermal collagen was obtained as non-pepsinized, acidified solution (stock concentration 4.0 mg/ml; CollagenG; Matrix Bioscience, Deutschland, Germany); rat tail collagen was non-pepsinized and acidified (stock concentration 3.95 mg/ml; Merck Millipore, Darmstadt, Germany). All experiments described in this article were performed using collagen from the same batch to avoid variability. Collagen mixes were prepared in a 50 ml conical tube with a total volume of 1 ml, keeping all reagents and pipet tips on ice to prevent the uncontrolled polymerization of the hydrogels. Polymerization was induced *in vitro* by raising the pH to 7.4 using 1 M NaOH (Sigma-Aldrich, Missouri, USA) and buffering by 0.36 M $NaHCO_3$ (Merck KGaA, Darmstadt, Germany), together with Dulbecco's modified Eagle's medium (DMEM, Gibco, ThermoFisher Scientific, Massachusetts, USA). The hydrogels were allowed to polymerize and equilibrate at 37°C for an hour.

2.2. Rheology tests: hydrogel viscoelastic properties

To explore the influence of collagen source and concentration of the hydrogels' mechanical properties, the elastic moduli of the different hydrogels were characterized by rheology tests using a stress-controlled rotational rheometer MCR 301 (Anton Paar, Gratz, Austria) at 37 °C with a standard steel cone geometry CP25–1 (25 mm of diameter and 1°). The hydrogels were prepared *in situ*, keeping their components at 4 °C until mixing to immediately loading in the rheometer in an injectable aqueous form. Approximately 200 µL of each hydrogel was placed in the Peltier plate's center, avoiding the insertion of air or bubbles. When centered, the cone plate was set to the corresponding gap height (48 µm), and silicone oil was applied on the peripheral to prevent evaporation. Initially, a time sweep was applied at 1 % strain and 1 Hz to monitor the gel polymerization through the evolution of the storage (G') and loss modulus (G") with time. Note that the strain level and frequency were set from preliminary strain and frequency sweeps in order to select values significantly lower than the yield strain, and greater than the crossover frequency, respectively. Once the viscoelastic properties were stabilized after approximately 45 min, a frequency sweep was applied by increasing the oscillatory frequency from 0.1 to 10 Hz at a shear amplitude of 1 % (10 Pt./dec). Then, the stored (G') and loss (G") moduli of each hydrogel were calculated as the average of the recorded data in the plateau (frequency range of 0.1–1 Hz). The complete rheometer data acquisition was performed using the software RHEOPLUS/32 (Anton Paar, Gratz, Austria). The shear modulus (G) was calculated from G' and G" using Rubber's elasticity theory [56]:

$$G = \sqrt{G'^2 + G''^2} \quad (1)$$

Finally, the elastic modulus (E) of the hydrogels was derived from the previous shear modulus (Eq. (2)).

$$E = 2G(1 + \nu) \quad (2)$$

where the Poisson's coefficient ν was assumed equal to 0.34, a value that was previously used in the literature for analogous hydrogels [57-59]. The number of samples for each case was $n = 3$. The results were established as the average among samples for

each hydrogel case. Finally, for a better understanding of the relative contributions of elastic vs. frictional forces to the overall rheological response of the hydrogel, the evolution of the loss or damping factor was calculated for previous frequency sweep using Eq. (3):

$$\tan\left(\delta\right) = \frac{G''}{G'} \quad (3)$$

2.3. Focused ion beam-scanning electron microscopy (FIB-SEM)

The morphology and micro/nano-architecture of all collagen hydrogels were characterized with focused ion beam milling and scanning electron microscope (FIB-SEM). For each type of hydrogel, 3 samples were analyzed ($n = 3$), 27 hydrogels in total. FIB-SEM methodology allows for the segmentation of a 3D fibered network and subsequent quantification of structural parameters, thereby overcoming common limitations such as 2D aggregations and overlapping of adjacent fibrils. After preparing 200 µL samples, they were fixed using 2.5 % glutaraldehyde in 0.1 M cacodylate-HCl buffer (pH 7.4) at 4 °C for 2 hrs. Immediately after that, fixed samples were rinsed three times in pure 0.1 M cacodylate-HCl buffer. The post-fixation consisted of incubating the sample at room temperature in the following solutions: 2 % osmium tetroxide and 1.5 % potassium ferrocyanide (1.5 hrs), 1 % thiocarbohydrazide (30 min), 2 % osmium (1 hr), 4 % uranyl acetate solution (10 hrs), 1 % lead aspartate (1 hr). Between steps, several washes in distilled water were performed. Lately, a dehydrated stepwise with acetone of increasing concentration was carried out (50–100 %) and an embedment in the hydrophobic Durcupan ACMTH resin (Sigma-Aldrich, Missouri, USA). The samples were glued with 2-component conductive resin to a conventional SEM pin stub, which was subsequently coated with 30 nm gold/palladium 80/20 to get a conductive surface.

Images were captured with the microscope Zeiss Crossbeam 550 (ZEISS, Oberkochen, Germany), which integrates a Xe/Ga ion source. A scheme of the FIB-SEM setup is shown in Scheme 1B. The microscope was tilted to achieve a 54º inclination between the SEM and FIB columns, whose FIB-SEM coincidence point was located at a working distance of about 5.2 mm. A 15×15 µm area was selected on the resin block's surface, and a 1-micron platinum protective layer was deposited using the electron beam for 5 min (Scheme 1B). In this layer, autotune and tracking marks are carved to minimize curtaining artifacts during FIB milling and correct misaligned sections in the post-processing. The FIB-SEM operates by slicing and polishing layers of the embedded hydrogel while capturing high-resolution images (Scheme 1C, pixel size 10×10 nm in xy and 20 nm in z) with the second beam using the software Zeiss Atlas 5 (ZEISS, Oberkochen, Germany). A video of the complete acquisition of the FIB-SEM for one of the collagenous hydrogels is available in the Supplemental Material (Video S1). Moreover, a comparison of the acquired microarchitectures for different collagen sources and concentrations is shown in Fig. S5.

2.4. FIB-SEM image analysis

Image stacks were analyzed using Avizo (Thermo Scientific, Waltham, Massachusetts, USA). A median filtering (3D interpretation, 18 neighbor pixels) was initially applied to reduce the noise while preserving the fiber edges. Then, an inner volume (6 × 6 × 6 µm) was selected as a volume of interest (VOI) to avoid the influence of the boundary faces. Small spots from remaining noise (<1000 pixels) were removed before calculation, and the fibers were interactively thresholded. An example of the resulting 3D collagen structure is displayed in Scheme 1D. Different microarchitectural parameters of the hydrogels were processed and calculated in the resulting fibered structure: the volume fraction as an indirect measure of the collagen density (module *Volume Fraction*); the degree of anisotropy, understood as the 3D fiber alignments along a particular directional axis (module *Degree of Anisotropy*); and the average fiber thickness and pore size of the VOI. To calculate the average fiber thickness and pore size of the structure, thickness maps, defined as the diameter of the largest ball containing the voxel and entirely inscribed in the thresholded region (fibers and spacing, respectively), were computed (module *Thickness Map*) following the definition given by Hildebrand & Rüegsegger [60]. Scheme 1D shows examples of these maps computed on one of the collagen hydrogels. Later, histograms of each distribution were calculated (module *Histogram*).

2.5. Cell culture and TFM experiments

Human MDA-MB-231 breast cancer cells were cultured (37ºC at 5 % CO2, humidified atmosphere) in DMEM with 4.5 g/L Glucose, l-Glutamine and Sodium Pyruvate (Gibco) supplemented with 10 % heat-inactivated fetal bovine serum (FBS; Gibco) and 1 % penicillin-streptomycin (Gibco). The cells were subcultured at approximately 90 % confluency and only used for experiments for passage numbers below 20. Before live cell fluorescence microscopy, MDA-MB-231 cells were labelled with CellTracker Green CMFDA (Invitrogen, Thermo Scientific, Waltham, Massachusetts, USA) and incubated with DMEM culture media at 37ºC for 1 hour.

Cells were detached with 0.05 % Trypsin/ EDTA (Gibco) and resuspended in fresh DMEM before added to the collagen mix at a density of 4×10^4 cells/mL, together with 5 µl of fluorescent microspheres (0.2 µm diameter, carboxylated, ex/em 660/680, Invitrogen). An amount of 20 µl of the mixture was pipetted in an imaging chamber (Secure-Seal hybridization sealing systems, Invitrogen) pre-mounted in a 35 mm petridish. The hydrogels with cells were allowed to polymerize in an incubator with 5 % CO_2 and 95 % humidity at 37ºC for a minimum of 1 h, before covering the dish with DMEM (containing FBS) to promote spontaneous cell migration.

2.6. TFM image acquisition and analysis

3D image stacks were acquired 24 hrs after collagen polymerization using a Leica Stellaris 8 confocal microscope (Leica Microsystems, Wetzlar, Germany) with a 20x glycerol immersion objective (NA 1.5). Approximately 30 µm z-stacks were acquired, adjusting the size to ensure the acquisition of the entire cell volume, with voxel size of 0.227 µm, 0.227 µm and 1.48 µm (x, y, and z, respectively). The cells labeled with CellTracker Green were excited at 498 nm (channel 1), while the dark red fluorescent beads were excited at 653 nm (channel 2). 16–19 cells were analyzed per group (n = 16–19 per group), a total of 157 cells. Examples of confocal images captured for cells embedded in each of the hydrogels studied are shown in Fig. S1 of the Supplementary Material. Then, Cytochalasin D (dissolved in DMSO, Sigma Aldrich) was added to a concentration of 4 µM and given at least 1 hr to relax the cells due to disruption of actin filaments. The same cells were imaged again to obtain comparative images in the absence of forces (stress-free state). A stage incubator was used to keep the cells at 37ºC and 5 % CO_2 during image acquisition.

The forces exerted by cells during maturation were quantified through 3D TFM experiments (see Scheme 2). To this end, 3D confocal imaged stacks at both stressed (Scheme 2A) and relaxed configurations (Scheme 2B) -previously filtered at different regions of interests (ROIs) and associated to different isolated cells- were used as an input for the open-source software TFMLAB [61]. As assumed in TFM methodology, we considered that hydrogels recover a stress-free state after cell relaxation. A study performed under

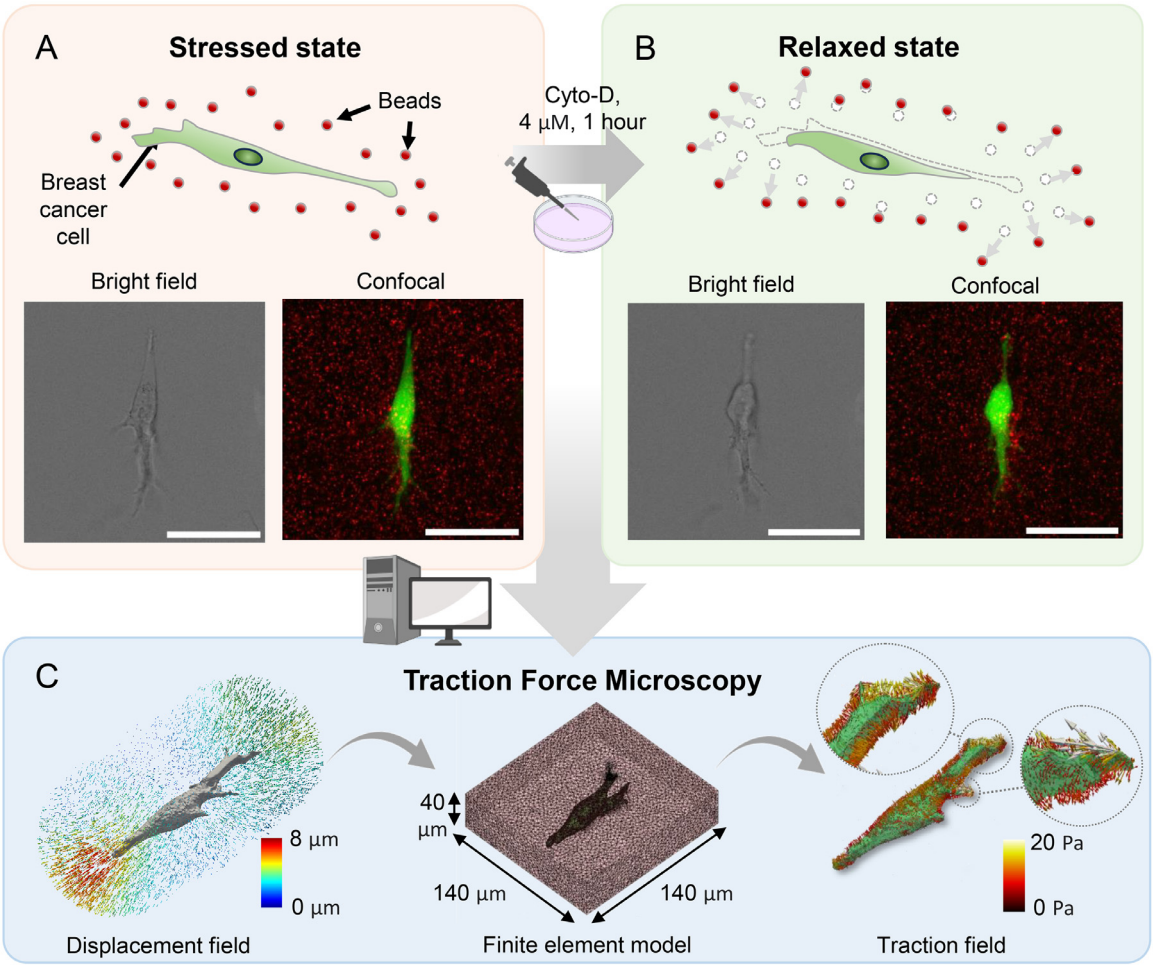

Scheme 2. An illustration of the 3D Traction Force Microscopy methodology in single breast cancer cells. A) A cancer cell is cultured on collagen hydrogel with embedded fluorescent microspheres. In the stressed state, the cell has exerted traction forces that deform the surrounding collagen network. B) After adding cytochalasin D (Cyto-D), their actin filaments are disrupted, and the cell returns to its original relaxed state. Thus, the fluorescent microspheres move to their original positions before deformation. As an example, the bright field and confocal images of both states for a single cell are shown. Scale bars are 50 µm. C) A displacement field is calculated by comparing the positions of the beads between the stressed and relaxed states. After solving a finite element model, the traction field that fits the measured microspheres' displacements is calculated numerically.

similar hydrogel composition and concentrations showed that assuming an elastic response of these hydrogels is a valid hypothesis [35], although this assumption is a common limitation for the recovery of tractions in TFM.

As shown in Scheme 2C, TFMLAB allows for confocal image processing, cell segmentation, and displacement measurement. In the image processing step, raw images were initially denoised using the penalized least-squares method. Image contrast was subsequently enhanced through stretching operations. Later, the software calculated a shift correction to adjust any microscope stage-related drifts. Cell bodies were segmented by applying Otsu's method for automatic image thresholding. Small binary objects not belonging to the cell body were also removed. In the following step, TFMLAB computes the displacement field in the selected ROIs using B-spline-based Free Form Deformation–based (FFD) image registration throughout a nonrigid mesh transformation from the stressed to the relaxed imaged configurations [62]. On the other hand, the Matlab toolbox *Iso2Mesh* was used to create a surface mesh of the cells from its confocal voxelised image. Then, a volumetric tetrahedral mesh of the hydrogel volume was created within the selected ROI. The FFD output displacement field values were interpolated from the image (voxel) coordinates to the FE nodes of the hydrogel and sprout boundary domains using the Matlab *griddedInterpolant* class with cubic interpolation. Then, using this displacement field as an input, cellular tractions are recovered along the boundary of the cell using an inverse formulation [61,63,64], that computes a consistent solution of stresses that fulfills equilibrium conditions within the hydrogel domain. The numerical implementation of the referred inverse formulation was implemented in TFMLAB software using Matlab. This code takes as an input the FE stiffness matrix computed from Abaqus Simulia, which is integrated in the workflow of the software. TFMLAB outputs (among other variables) displacement and traction fields along the cell boundary. The magnitude of these fields is used to quantify the mechanical activity of the breast cancer cells in the different analyzed hydrogel compositions. From the .vtk files provided by TFMLAB, 3D-renders of the cells, displacement and traction fields were created using the open-source software ParaView (Sandia National Laboratories, Kitware Inc, Los Alamos National Laboratory) for visualization. The latest version of the TFMLAB code can be downloaded from https://gitlab.kuleuven.be/MAtrix/Jorge/tfmlab_public.

The overall specific strain energy exerted by cells was also computed, as a measure of the internal work developed by cells to externally deform their surrounding collagen mechanical microenvironment. The specific strain energy was calculated as follows:

$$Energy = \frac{1}{\sum A_i} \sum t_i \cdot u_i \cdot A_i \quad (4)$$

with $\boldsymbol{t}_i$ and $\boldsymbol{u}_i$ being the traction and displacement vectors, respectively, computed at the centroid of the facets i of the surface mesh of the cell. A_i is the area of the facet i.

Tractions were further post-processed to obtain the traction polarity using the following approach. First, the traction vectors with magnitude above 90-percentile on the cell surface were selected. Then, the eigenvalues of these vectors were computed using functions `cov` and `eig` from Matlab. The polarity of the traction field P was finally computed with the following equation:

$$P = \frac{E_1}{E_1 + E_2 + E_3} \tag{5}$$

where E_1, E_2, E_3 are the traction eigenvalues sorted in descending order. P has a value between 0 (non-polarized) and 1 (completely polarized).

2.7. Morphological characterization of the cells

From the cell segmentations provided by TFMLAB, we computed the following morphological operations:

$$Cell\ Volume = N_c \cdot V_{vox} \tag{6}$$

where N_c is the number of voxels in the cell binary mask and V_{vox} is the physical volume of one image voxel ($\sim$0.08 μm^3).

Cell protrusion segmentation was performed as previously described (Yuan et al., 2023). Briefly, the largest sphere that fits within the cell binary mask was calculated using MATLAB functions `bwdist` and `pdist2`. We then selected the voxels from the cell binary mask located at a Euclidean distance larger than two times the sphere radius. Connected components of this selection were taken as individual protrusions. The principal axis length of these protrusions was then obtained with function `regionprops3`. Moreover, this function also provided the 'solidity' metric of the cells. In this work, we referred to the solidity of the cells as "sphericity" and expressed it between 0 and 1 (perfect sphere).

2.8. Statistical analysis

The significant differences in cell's tractions, energy, traction polarity, or hydrogel's elastic modulus among the different hydrogels were evaluated using one-way ANOVA Tukey's test in MATLAB (function `anova1`).

3. Results and discussion

3.1. Quantitative atlas of structural and mechanical features of collagen hydrogels

The interaction between cells and their ECM is intricately linked to the complex microarchitecture and physicochemical characteristics of the environment [17]. These factors influence the cells' ability to exert traction forces, affecting the manner and speed of migration [65]. In this context, substrate viscoelasticity is an important property that affects hydrogel response to traction exerted by the cells on the polymer network during 3D migration [66], which is governed by a combination of matrix pore size, degradability and viscoplasticity [12,13]. On the other hand, tunable hydrogels provide a platform to explore the impact of the micromechanical and microstructural features of 3D matrices on cell behavior. The present work is, to our knowledge, unique in comparing the mechanobiology of cancer cells in ECM with a wide range of compositions, collagen concentrations, and, subsequently, physicochemical microenvironments.

Mechanical properties of collagen ECMs are determined by the fibril density, spatial orientation of the fibers, and their degree of crosslinking [67,68]. Polymerization conditions can be varied to obtain mechanically distinct ECMs with different fibrillar microstructures. The nine hydrogel conditions explored in this study (BOV, RAT and MIX at collagen concentrations of 0.8, 1.5, or 2.5 mg/ml) were mechanically characterized after polymerization using shear rheology ($n = 3$ per case) to obtain the storage modulus (G'), loss modulus (G") and elastic modulus (E), as shown in Fig. 1A-C and Table 1 of the Supplementary Material. Fig. S2 provides the results of the initial time and frequency sweeps to check the hydrogel polymerization (average curve per case), as described in Materials and Methods. Note that the absence of significant differences in mechanical properties after the addition of the fluorescent microspheres or with incubation time after polymerization ($\sim$45 min) was also verified, as shown in Fig. S3 of the Supplementary Material. While G' modulus describes the general elasticity of the hydrogel, the G" modulus reflects the dissipated energy as a characteristic viscosity. In all cases, G' was higher than G" (Fig. 1A-B). Fig. 1D-F show the evolution of the damping factor of the hydrogels made with a collagen concentration of 0.8, 1.5 and 2.3 mg/ml at different frequencies (0.1–10 Hz), respectively. The loss factor remains mostly below 0.2 in all hydrogels, reporting a clear contribution of elastic forces over internal friction between the components in the flowing hydrogel. Nevertheless, the hydrogel based on bovine collagen at its lowest concentration (BOV 0.8 mg/ml) reported a loss factor around 0.25 for frequencies between 0.1 and 1 Hz, as shown in Fig. 1D. Understanding this factor as the ratio of energy dissipated per cycle to the maximum stored energy, the stored elastic energy dissipated through viscoelastic processes cannot be considered negligible in this softest hydrogel. Despite this case, our collagen-based hydrogels predominantly exhibit solid mechanical behavior rather than fluid-like characteristics. Previous studies in other type I collagen gels reported that rheological parameters (G' and G") increased with the fibrillar concentration [69]. In our study, this relationship was also proven to be independent of the collagen source and stiffness. The elastic moduli of the hydrogels were significantly different at lower versus higher concentrations of collagen (see Fig. 1C and Fig. S4 of the Supplementary Material). Rat tail collagen-based hydrogels also presented a higher elastic modulus than both bovine dermis- and mixed collagen-based hydrogels in any concentration. For instance, 2.3 mg/ml of rat tail collagen provided an elastic modulus to the hydrogels of 240.1 ± 39.4 Pa, 25 times stiffer than the one measured in the 0.8 mg/ml bovine dermis collagen-based gels (9.3 ± 4.7 Pa). Such differences in stiffness between rat-tail and bovine collagen-based lattices align with measurements carried out in previous studies using atomic force microscopy [17].

Next, comparing the fibrillar microstructure of the nine collagen hydrogels using scanning electron microscope (SEM) images (Fig. 1G) showed that the pore size visibly decreased with increasing collagen concentration when using any collagen source. Further, a qualitative observation of the SEM images (Fig. 1G) suggests that the bovine dermis collagen matrix showed entangled node-like fibers, whereas the rat tail collagen-based structures presented well-defined and more homogeneous pores. These results are consistent with other gels made of similar types of collagens [70], suggesting that the network of pure bovine dermis collagen, and to a lesser extent of the mixed collagen, is more heterogeneous than that of pure rat tail collagen. One plausible explanation for this could be the difference in the species and the tissue from which the collagens are extracted [71].

FIB-SEM was used to quantify how the different structural properties affect the nanoarchitecture of the hydrogel (Scheme 1B-C). Fig. 1H shows an example of the evolution of the fibered structure with the collagen concentration for bovine dermis hydrogels. While FIB-SEM has previously been applied to hydrogels for fiber-tracing [72], to our knowledge, the effects of 3D structural prop-

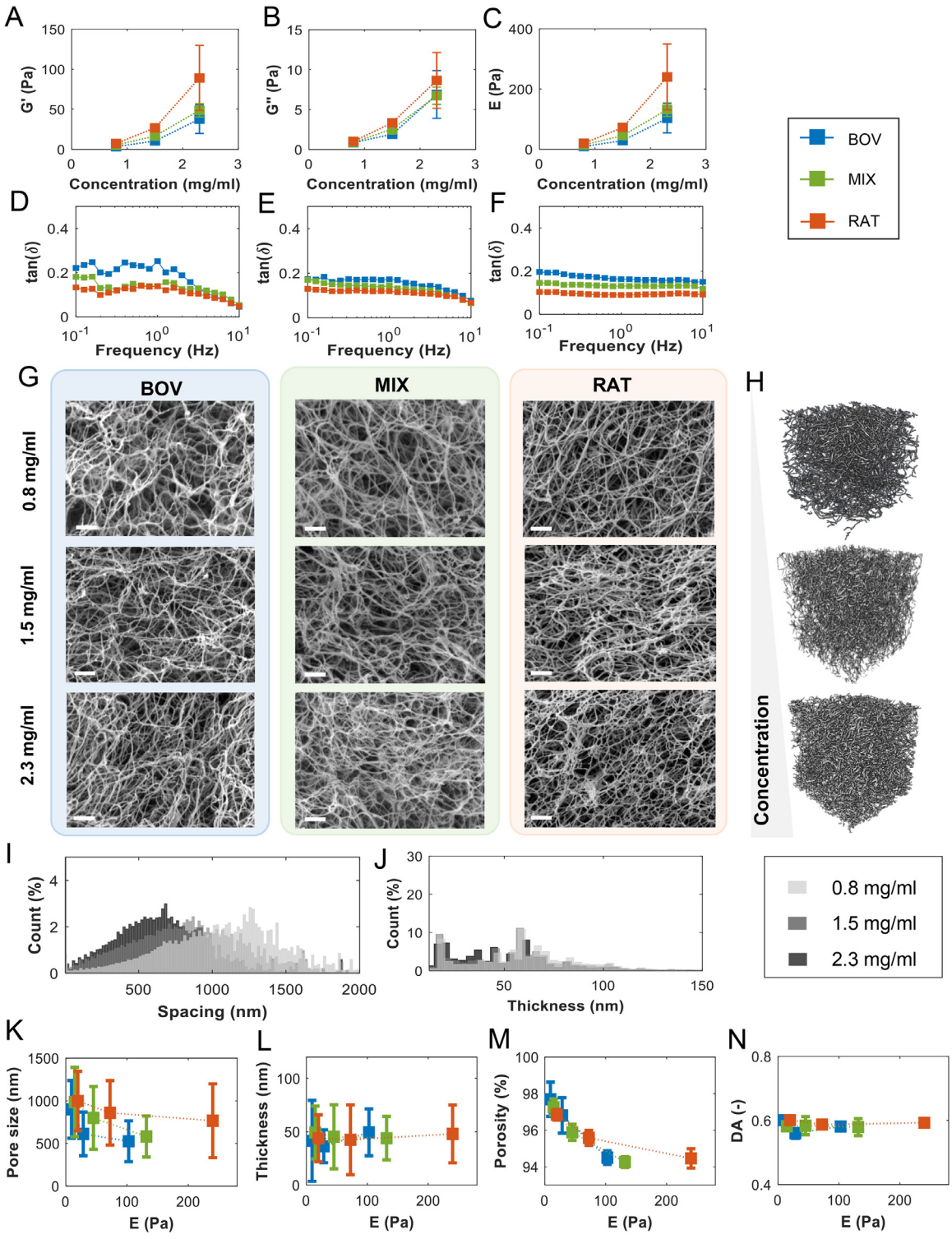

Fig. 1. Mechanical and structural characterization of the hydrogels prepared with several collagen compositions and concentration. Evolution of the: A) storage modulus (G'); B) loss modulus (G''); and C) apparent elastic modulus (E) for each collagen source (bovine dermis-based, BOV, rat tail-based, RAT, and mixed collagen) and concentration (0.8, 1.5 and 2.3 mg/ml) ($n = 3$). The degree of significance between groups (p-values) are reported in Fig. S4. Average evolution of the damping factor during a frequency sweep (strain γ 1%, frequency 0.1–10 Hz) in hydrogels with a collagen concentration of D) 0.8 mg/ml; E) 1.5 mg/ml; and F) 2.3 mg/ml. G) SEM images of each hydrogel. Scale bar is 1 μm. H) Evolution of the 3D fibered structure reconstructed by FIB-SEM with the collagen concentration (BOV case). I-J) Examples of the pore size (spacing) and fiber thickness distributions in RAT hydrogel at different concentrations. K-N) Relationship between microstructural parameters, K) pore size; L) fiber thickness; M) porosity; and N) degree of anisotropy with the apparent elastic modulus of hydrogels ($n = 3$).

erties on the apparent mechanics of the matrix and the cellular mechanical interaction are studied for hydrogels from different collagen sources and concentrations for the first time. Fig. 1I-J show an example of the pore size and fiber thickness distributions (histograms) in pure rat tail collagen. The observed pore size was highly dependent on the collagen concentration, in line with what is observed in the 3D reconstructions of the Fig. 1H. Further, Fig. 1K-L quantifies the mean and standard deviation of the pore size and thickness in all collagen sources and concentrations. As shown in Fig. 1K, slightly larger pore sizes were found in rat tail collagen-based hydrogels, suggesting that pore size also depends on the collagen source of the matrix and consequently on its physicochemistry. Meanwhile, fiber thickness was not influenced by a change in concentration or collagen source, with an average thickness of around 50 nm across all hydrogels (Fig. 1L). This is consistent with the 3D structural analysis of the purified tendon collagen-based gels [72], where the fiber thickness distribution was modulated only with changes in polymerization temperature or upon addition of proteoglycan decorin.

Fig. 1K-N also compare the mean elastic modulus of the nine hydrogels with the quantitative structural data measured by FIB-SEM, including the mean pore size (Fig. 1K), the mean fiber thickness (Fig. 1L), the porosity (Fig. 1M), or the degree of anisotropy (Fig. 1N). Porosity consistently decreased with the hydrogel stiffness for all three types of hydrogels. This observation aligns with the theory of micromechanics, where stiffness decays with porosity in lattice/cellular materials [73]. It is also consistent with the SEM images (Fig. 1G) and previous studies [74]. Mean fiber thickness and the degree of anisotropy of the structure (around 0.58 in all cases) did not significantly influence their bulk mechanical properties. The slight anisotropy of the structure is likely due to the manufacturing and polymerization methodology of the samples or their preparation for the FIB-SEM. However, this parameter does not seem to play a critical role in the stiffening of the gel. Therefore, the mechanical properties of our hydrogels are likely regulated by the combination of porosity, pore size, physicochemical differences in crosslinking, and the intrinsic elastic modulus of the collagen fibers. For reference, the elastic moduli of detonated fibrils from bovine and rat tail tendons are reported to be approximately 5 GPa and 11 GPa, respectively [75,76].

In summary, the diverse hydrogel environments examined in this study inherently introduce varying ECM pore size, porosity and apparent mechanical properties to the cultured cells. For a given fiber size and degree of structural anisotropy, hydrogels prepared from bovine dermis collagen exhibit more heterogeneous fibrous structures, resulting in smaller pore sizes and lower porosity than their rat tail-based counterparts. However, the elasticity of the latter imparts greater mechanical resistance for cell interactions. Hydrogels composed of both collagen types present intermediate structural and mechanical properties, with collagen concentration regulating their nanoarchitecture. It is known that breast cancer cells remodel the ECM by altering its structure and mechanics. The ECM becomes disorganized and deregulated as a result of the increasing fiber density and stiffness during tumor progression [77]. We next delve into a detailed analysis of how these distinct environments influence both the initial phenotypic and mechanical behavior of isolated cancer cells.

3.2. The mesenchymal phenotype of cancer cells is independent of the matrix nanoarchitecture

Cell morphological parameters were compared across each type of hydrogel (n = 16–19, Fig. 2A), including the number of protrusions (Fig. 2B), the degree of sphericity (Fig. 2C), the cell volume (Fig. 2D), the cell length (Fig. 2E), and the average protrusion length (Fig. 2F). No significant differences were found between groups in any of these parameters. Regardless of the stiffness, structural or physicochemical composition of the hydrogel, the cells generally adopted an elongated spindle-like morphology with one or two protrusions, as indicated by the consistent number of protrusions (around 2 in all cases, Fig. 2B) and sphericity (around 0.6, Fig. 2C). This elongated morphology (Fig. 2A) is associated with a mesenchymal-like invasion, a migration mechanism dependent on actin-based protrusions and ECM adherence via cellular receptors including integrins [78-81]. The mesenchymal phenotype evident in confocal images (Fig. S1 of the Supplementary Material) aligns with the morphology adopted by MDA-MB-231 cells during migration through the ECM in 3D models of varied pore sizes and is a typical feature of aggressive tumor cells *in vivo*, contrasting the spherical shape of non-invasive cells [78-80].

Interestingly, this mesenchymal-like morphology is observed across all studied collagen compositions without significant differences. In this regard, it was described that MDA-MB-231 cells invaded polymerized type I collagen hydrogels with telopeptides, in contrast to the less invasive cell line MDA-MB-435S that showed a spindled form only in telopeptide-free collagen [78]. On the other hand, other authors observed the same spindle shape in MDA-MB-231 in different collagen types [26] but also described greater sphericity in bovine dermis collagen, a morphology associated with ameboid-like migration [74]. However, sphericity in our study (Fig. 2C) showed no significant differences across all nine types and concentrations of hydrogels. Consistent trends were observed in cell volume (Fig. 2D, 6291.9 ± 3050.1 μm^3), cell length (Fig. 2E, 61.1 ± 21.2 μm), and average protrusion length (Fig. 2F, 24.8 ± 13.9 μm), with no clear variations or significant differences in any of these parameters. In the same cell line and mixed collagen hydrogels (BOV+RAT at a ratio of 1:1), Steinwachs et al. [35] did find significant differences in cell elongation, but only when slightly higher and lower collagen concentration, 0.6 and 2.4 mg/ml, were compared.

These results suggest that the explored mechanical and structural microenvironment does not alter the morphology of this cell line. Consequently, our breast cancer cells were capable of elongating and generating protrusions independent of the pore size of the surrounding collagen matrix and the elasticity of the fibers, suggesting comparable mesenchymal migrations. Thus, these microenvironments did not present a significant barrier to the cells imposed by the matrix in adopting an invasive and aggressive morphology. As proof of their migratory capacity, Video S2 of the Supplementary Material shows the behavior of cells in mixed collagen hydrogel at the concentration of 1.5 mg/ml for 72 hrs.

3.3. 3D cellular forces and energy describes a linear response and plateau with the ECM stiffness

In order to explore the influence of the microenvironment on cell-ECM mechanical interactions, we used TFM to measure cell-induced matrix displacements and tractions. Fig. 3A shows the displacement fields around nine representative cells for each hydrogel type and concentration. Differences can be observed as a function of the collagen concentration, where the displacement magnitude slightly decreases as the concentration increases. In all cases, maximum matrix displacements were located around the tips of cells' protrusions. Fig. 3 also shows the change in 90-percentile displacements generated around the cells' surface for each hydrogel (n = 16–19) as a function of collagen concentration (Fig. 3B) or the ECM's elastic modulus (Fig. 3C). The degrees of significance in the 90-percentile displacements between groups are provided in Fig. S4 of the Supplementary Material. Consistent with previous results, we observed a general decrease in cell-generated displacements as the collagen concentration or the hydrogels' stiffness increases. However, according to Fig. S4, these differences were more statis-

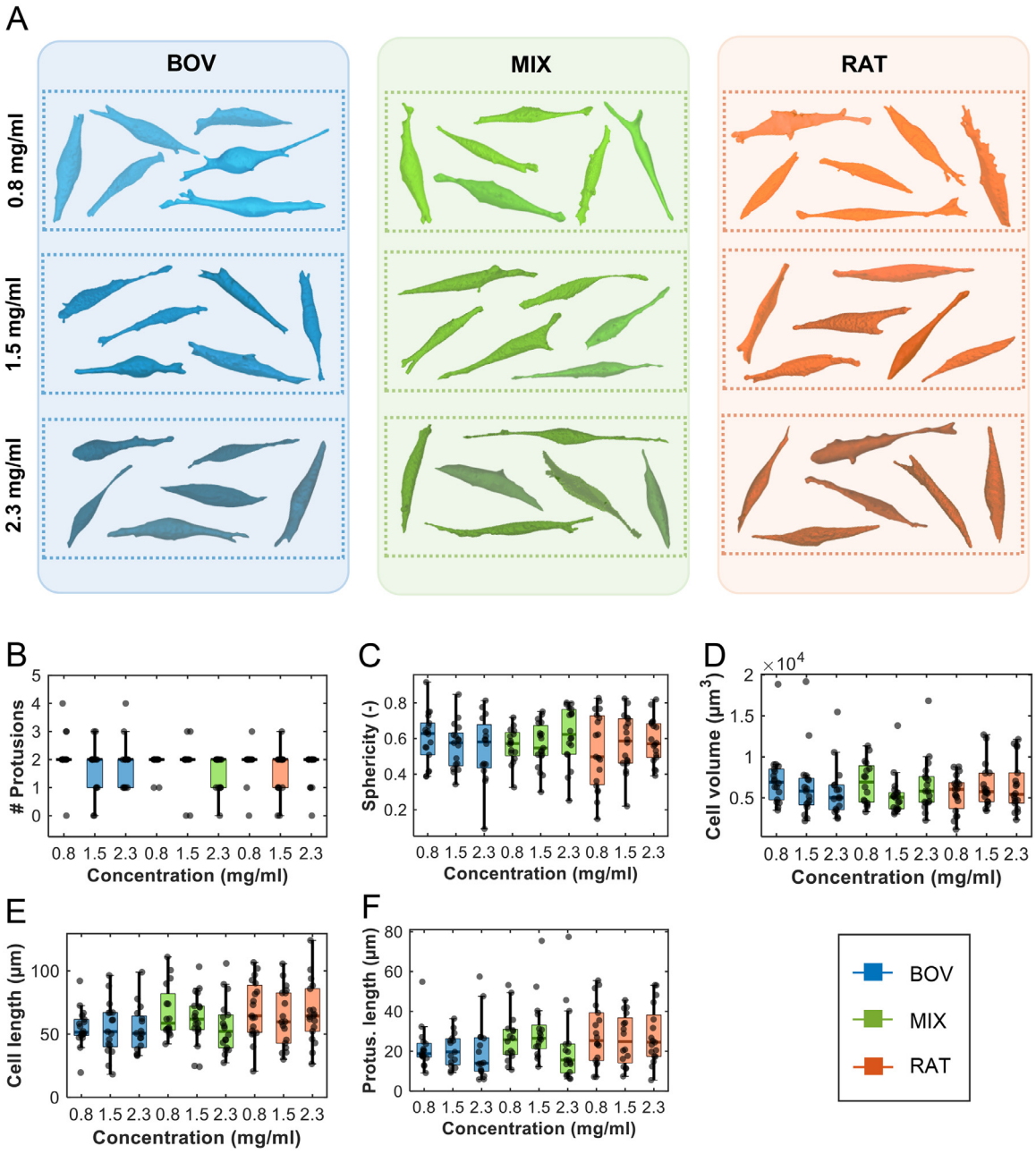

Fig. 2. Morphology of the breast cancer cells embedded in the collagen hydrogels. A) Rendering of some representative analyzed cells in the different hydrogels. B) Number of protrusions, C) degree of sphericity, D) cell volume, E) cell length, and F) average protrusion length, reported as a boxplot per collagen source (bovine dermis-based, BOV; rat tail-based, RAT, and mixed collagen) and concentration (0.8, 1.5, and 2.3 mg/ml). No statistical differences were found (n = 16–19).

tically significant when comparing the hydrogels made of bovine dermis collagen (BOV) at concentrations of 0.8 and 1.5 mg/ml with the 90-percentile displacements computed in the rest of the matrices. These displacements are a result of tractions that cells exert to maintain their shape, reorganize the extracellular matrix, migrate, or communicate with nearby cells [24,25]. Traction fields visualized around protrusions of individual cells for each hydrogel condition show that cells exert pulling forces using their protrusions to deform the surrounding hydrogel (Fig. 4A). Fig. 4B shows the 90-percentile tractions as a function of the collagen concentration (mg/ml) for each composition. In contrast to the displacements, tractions increase with collagen concentration from ~3 Pa in the softest gels to ~65 Pa in the stiffest ones with significant differences (p-value < 0.001, Fig. S4). Fig. 4E shows the relationship between the tractions and mean elastic modulus measured using rheological tests. These results suggest that the strength with which a cell pulls the collagen substrate is strongly dependent and increases with the stiffness of the hydrogel.

As the stiffness of the base collagen source was higher, the increase in the mean 90-percentile traction was smaller between the lowest and highest concentration, being approximately 11-fold, 9-fold and 7-fold for the bovine dermis, mixed and rat tail collagenous hydrogels, respectively. Moreover, fixing a collagen concentration, notable differences were also found between collagen sources (Fig. S4), possibly due to the different stiffening profiles of each collagen type. The increase in cell traction or cell stiffness with ECM stiffness was previously observed in 2D experiments in other cell lines, for example, in human mesenchymal cells on collagen-coated substrates [82], in vascular smooth muscle and endothelial cells in polyacrylamide gels [83,84], in fibroblasts [21,85], or

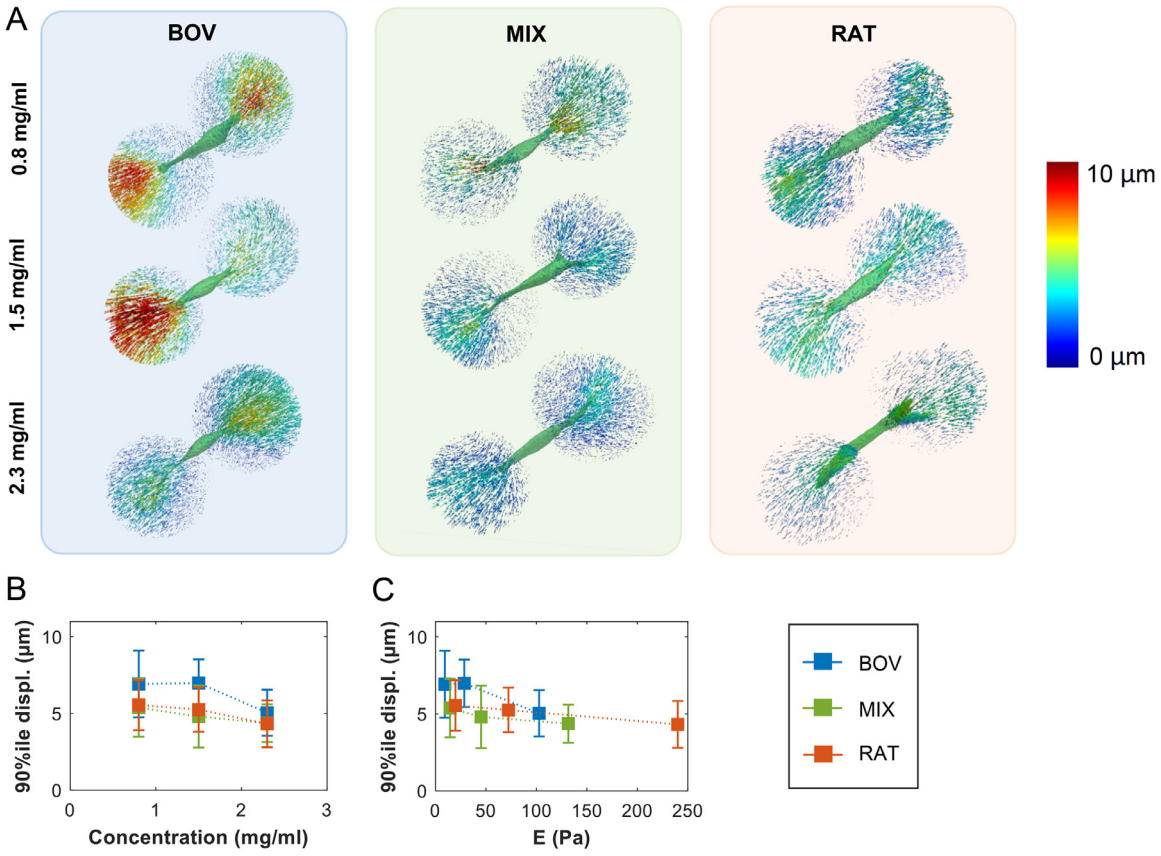

Fig. 3. Displacement field in the extracellular matrix calculated by Traction Force Microscopy due to tractions exerted by MDA-MB-231 breast cancer cells. A) One sample cell is shown for each hydrogel composition (bovine dermis collagen, BOV; mixed collagen, MIX; rat tail collagen, RAT) and collagen concentration (C = 0.8, 1.5 and 2.3 mg/ml). Evolution of the 90-percentile displacement with B) the collagen concentration, and C) the hydrogel's apparent elastic modulus (mean value). The degrees of significance between groups (*p*-values) are reported in Fig. S4.

in human metastatic breast, prostate and lung cancer cell lines [86]. This behavior could be due to strain-control mechanisms, where the cell applies a fixed deformation on its environment to mechanosense, migrate, or interact with surrounding cells [87,88]. In 3D environments, cell–ECM strain dynamics have been reported to be cell type-dependent. MDA-MB-231 cells produce low ECM strains in 3D collagen [89]. Different studies describe (a) nearly constant forces with increasing stiffness of the hydrogel [35] or (b) cell-generated force increase with initial collagen matrix stiffness [26]. These differences may be due to the different microstructure characteristics of the matrix or the different migration mode of the individual cells. In contrast, mesenchymal fibroblasts generate anisotropic ECM strains nearly four-fold higher than breast cancer cells [89,90]. Anguiano et al. [91] showed that H1299 lung cancer cell tractions also increase with higher substrate (mixed collagen-Matrigel hydrogels) stiffness. As a result, the exerted tractions to achieve a given deformation in stiffer microenvironments should be higher. This hypothesis is consistent with our observed displacement fields (Fig. 3), where not many significant differences were found between the analyzed cases, as reported in Fig. S4 of the Supplementary Material. Further, the mesenchymal-like elongated morphology of the cells seen for all the analyzed cases suggests that cells maintain a consistent and optimal morphology to mechanosense the hydrogel.

As shown in Fig. 4E, it is also interesting to note that traction forces exerted by the cancer cells seem to have a tendency for saturation at a hydrogel stiffness of 70–80 Pa, after which a stiffness-dependent increase in tractions is curved. This force saturation is seen in the changes in the traction growth slopes of the cases with the highest collagen concentration, especially in the stiffest ECM tested in the study (RAT 2.3 mg/ml), whose elastic modulus was above 200 Pa. Fig. 4C plots the strain energy (normalized to its surface area) applied by the cell during its mechanical interaction with the ECM. The strain energy is plotted against the hydrogel stiffness for each collagen composition and concentration (Fig. 4F). We found that the strain energy also seems to reach an asymptote ~40 Pa•µm in rigid mechanical microenvironments. This conclusion was supported by the lower significant differences found in energy between matrices with highest apparent stiffness: BOV 2.3, MIX 2.3, and RAT 1.5 mg/ml and RAT 2.3 mg/ml (Fig. S4). Similar conclusions have previously been derived for tractions *in silico* [92]. These results also agree with a previous study in a 2D model where average traction forces of fibroblasts and epithelial cells varied linearly with the hydrogel's stiffness up to a force saturation level, which was an intrinsic property of each cell line [85]. However, to our knowledge, this is the first time a mechanical limit has been quantified in a 3D *in vitro* system with cancer cells for both cell tractions and strain energy. This phenomenon may be due to the appearance of a cell's physiological mechanical and energetic limit after reaching a saturation in its internal stiffness and strain energy, as was found in previous *in vitro* studies [21].

The strain energy distribution around mesenchymal-like cells was demonstrated to increase the complexity and anisotropy of traction force generation. This phenomenon is closely related to cell morphology reported in the previous section, suggesting that the directionality of tractions, not their magnitude, may be essential for cancer invasion [80]. Fig. 4D and G show the traction polarity plotted against collagen concentration and mean elastic mod-

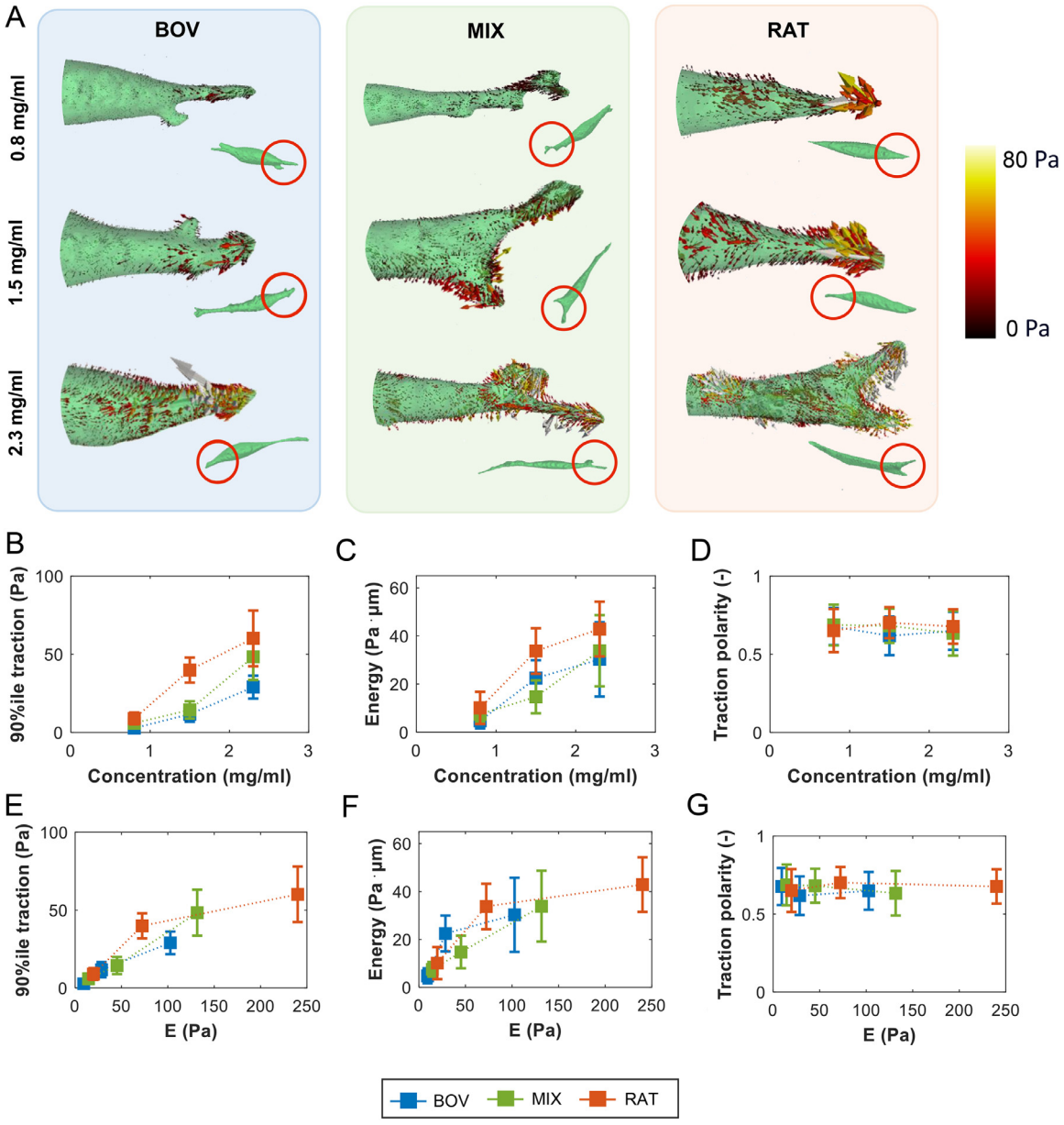

Fig. 4. Mechanical interaction between the breast cancer cells and the different explored microenviroments. A) Traction field exerted by MDA-MB-231 breast cancer cells on their extracellular matrix 24 hrs after seeding, calculated using Traction Force Microscopy. Tractions in one protrusion of a sample cell are presented for each hydrogel composition (bovine dermis-based collagen, BOV; mixed collagen, MIX; rat tail-based collagen, RAT) and collagen concentration 0.8, 1.5 and 2.3 mg/ml). B-G) Relationship between the 90-percentile traction, the cellular specific strain energy and the traction polarity with the collagen concentration (B-D) and the hydrogel's apparent elastic modulus (mean value, E-G). The results are presented as mean ± standard deviation (n = 16–19). The degrees of significance between groups (p-values) are reported in Fig. S4.

ulus, respectively. There is no significant trend, and it stabilizes around 0.6–0.7 with no significant differences across all nine hydrogels (p-values > 0.05 in most cases, see Fig. S4). These results are in the line of previous studies in the same cell line, but that only analyzed mixed collagen hydrogels at a ratio of 1:1 [35]. This suggested that breast cancer cells adopt a similar polarity with a high anisotropy regardless of the apparent mechanical properties of their ECM.

In brief, cells exert polarized forces in a preferred direction whose magnitude increases linearly with the stiffness of the matrix up to a physiological traction/strain energy limit. Whether this level of rigidity represents a real space restriction to the invasive or migratory activity of the cells or if they end up locally deforming or degrading the matrix exceeds the scope of this work. In the following subsection, the potential influence of the structural parameters of the collagenous structure of the hydrogel on these mechanical parameters is discussed.

3.4. ECM micro and nanoarchitecture: a key modulator for 3D cellular tractions

To investigate whether traction forces and energy rely on the ECM microarchitecture parameters and/or on the collagen-type nature of the ECM, we plotted in Fig. 5A-B and D-E the trends of the traction field and specific strain energy with pore size and porosity for the different collagen-based hydrogel types and concentrations. For the three types of hydrogels, it can be observed that the traction field and strain energy are highly dependent on the pore size

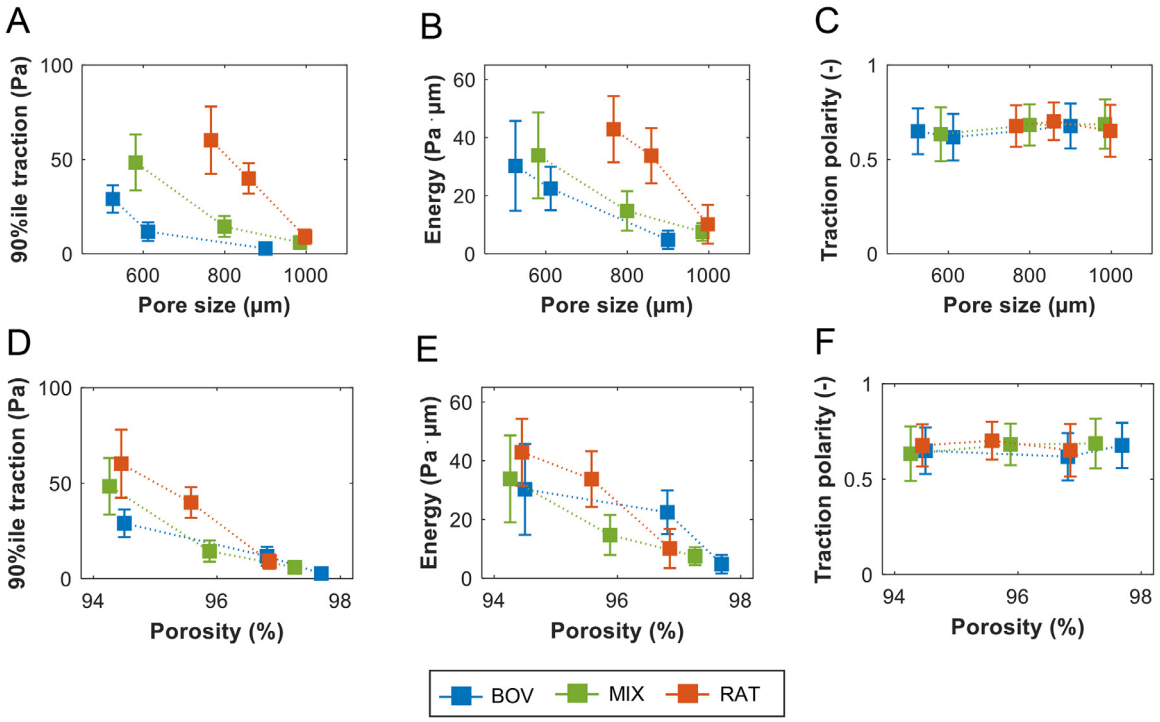

Fig. 5. Evolution of the 90-percentile traction, the cellular specific strain energy and the traction polarity with the hydrogel's fibered structure. Relationship with A-C the pore size in the collagen network and D-F the porosity of the collagen structure. The evolution for all collagen compositions (bovine dermis-based, BOV; mixed, MIX; and rat tail-based, RAT) are presented. The results are presented as mean ± standard deviation (n = 16–19).

and porosity and decrease inversely with them. This finding agrees with several studies that have demonstrated changes in the cell's mechanical behavior and cell migration as a result of the pore size [93]. Cell migration is directly related to the ability of the cells to generate traction forces, the migration speed being negatively correlated with the traction forces with a Hill-curve shape [94]. Another study reported that migration in the absence of space restrictions declines as a linear function of the matrix's pore size, which was controlled by the collagen composition and the polymerization temperature [95]. However, the pore size was measured through 2D scanning/ transmission electron microscopy images, thus precluding the direct assessment of the 3D extracellular matrix.

In addition, both traction forces and strain energy are highly dependent on the physicochemical characteristics of the hydrogels. As seen in Fig. 5A-B and Fig. 5D-E, for a given porosity percentage or pore size, tractions and strain energy are higher in the rat-based hydrogel (RAT, stiffest case) and lower values in the bovine one (BOV, softest case). These results suggest that cells modulate forces to deform the hydrogel depending on the microstructure and physical impedance found along their 3D migration path, characterized in our study by hydrogels' stiffness and microstructural properties. In addition to this, when cells contract the ECM, they exert both adhesion and resistant forces that do not depend only on the stiffness of the matrix but also on the physicochemistry and protein concentration of the polymeric network, the adhesion ligand density and nanoarchitecture (aminoacidic sequences of collagen) [81,96]. Stiffer matrices also appear to impact the level of integrins expression, causing a bidirectional signaling with cell traction forces. Increased matrix stiffness also enhances focal adhesion assembly, affecting cell spreading and migration [97,98].

According to Fig. 5C and F, the traction polarity also remains stable in all fibrous structures. As with the global stiffness of the ECM, the fiber density and the pore size do not represent a barrier for the cell to mechanically interact with its ECM clearly in a polarized manner. Nevertheless, the magnitude must be higher to deform fibered structures with lower porosities. This further supports the cellular preference for an elongated morphology with two protrusions and a spindle shape described earlier, regardless of the surrounding structural or mechanical microenvironment to which it is subjected.

4. Conclusions

In conclusion, this study shows the combination of 3D TFM and FIB-SEM techniques as a valuable methodology to better correlate cell mechanical behavior with the structural properties of collagen ECMs. As far as the authors knowledge, there is no study that analyzes the impact of the physicochemical and morphological properties with resolution at the nanoscale of a wide variety of natural three-dimensional collagen networks on the mechanical behavior of breast cancer cells in a single *in vitro* model. In particular, we employed well-characterized tunable collagen-based hydrogels to model several extracellular natural microenvironments with varied mechanical properties and fibrillar microarchitectures. While bovine dermis-based collagenous hydrogels provide structures with lower porosity and pore size, rat tail collagen provides greater bulk mechanical properties to the gel. The mechano-structural differences in these matrices are due to the elasticity of each collagen type and different physical crosslinking methods. In these ECMs, we investigated the MDA-MB-231 cells' morphology after 24 hrs of culture into each hydrogel, their mechanical behavior (tractions exerted by the cellular actin-myosin system, strain energy, and traction polarity), and its relationship with mechanical and structural properties of the matrices. Our results provide evidence that the mechanical and structural microenvironments do not influence the morphology of the cells. In all cases, cancer cells developed an elongated spindle-like shape without significant changes in volume, cell length, or average protrusion length, similar to mesenchymal-like invasive phenotype. The tractions and specific strain energy exerted by the cancer cells followed a linear

response and plateau with the stiffening of its ECM, reaching saturation in hydrogels with high apparent elastic moduli (> 200 Pa). An increase in the porosity percentage or pore size of the collagenous substrate was demonstrated to also impact the mechanical behavior of the cancer cells by reducing the force and energy they applied to pull and deform the fibered network. This is also reflected in the high traction polarity, with no significant differences observed across all studied ECMs. With all these results in hands, we hypothesize that MDA-MB-231 breast cancer cells tune their mechanical state and subsequent deformation of the hydrogel to maintain their migration and invasiveness capacities. This methodology could also be applicable to other cell lines to investigate mechanobiological differences between cancer and non-tumor cells, as well as to understand the factors that favor their proliferation and/or migration.

Declaration of competing interest

The authors declare that they have no known competing financial interests or personal relationships that could have appeared to influence the work reported in this paper.

CRediT authorship contribution statement

Raquel Ruiz-Mateos: Writing – review & editing, Writing – original draft, Visualization, Investigation, Formal analysis, Data curation. **Jorge Barrasa-Fano:** Writing – review & editing, Writing – original draft, Software, Formal analysis, Data curation. **Apeksha Shapeti:** Validation, Resources, Methodology, Formal analysis, Data curation. **José Enrique Martín-Alfonso:** Validation, Supervision, Methodology. **Jaime Domínguez:** Visualization, Supervision, Resources. **Hans Van Oosterwyck:** Validation, Supervision, Resources, Methodology. **Esther Reina-Romo:** Writing – review & editing, Writing – original draft, Validation, Supervision, Resources, Project administration, Methodology, Investigation, Funding acquisition, Formal analysis, Conceptualization. **José Antonio Sanz-Herrera:** Writing – review & editing, Writing – original draft, Validation, Supervision, Resources, Project administration, Methodology, Investigation, Funding acquisition, Conceptualization.

Acknowledgments

This work was supported by MCIN/AEI/10.13039/501100011033 [PID2020-113790RB-I00, PID2021-126051OB-C42].

Supplementary materials

Supplementary material associated with this article can be found, in the online version, at doi:10.1016/j.actbio.2024.07.002.

References

[1] H. Sung, J. Ferlay, R.L. Siegel, M. Laversanne, I. Soerjomataram, A. Jemal, F. Bray, Global Cancer Statistics 2020: GLOBOCAN estimates of incidence and mortality worldwide for 36 cancers in 185 countries, CA Cancer J. Clin. 71 (2021) 209–249, doi:10.3322/caac.21660.
[2] A. Malandrino, M. Mak, R.D. Kamm, E. Moeendarbary, Complex mechanics of the heterogeneous extracellular matrix in cancer, Extreme Mech. Lett. 21 (2018) 25–34, doi:10.1016/j.eml.2018.02.003.
[3] M.W. Pickup, J.K. Mouw, V.M. Weaver, The extracellular matrix modulates the hallmarks of cancer, EMBO Rep. 15 (2014) 1243–1253, doi:10.15252/embr.201439246.
[4] T.R. Cox, The matrix in cancer, Nat. Rev. Cancer 21 (2021) 217–238, doi:10.1038/s41568-020-00329-7.
[5] R.O. Hynes, The extracellular matrix: not just pretty fibrils, Science 326 (2009) 1216–1219, doi:10.1126/science.1176009.
[6] S. Ozbek, P.G. Balasubramanian, R. Chiquet-Ehrismann, R.P. Tucker, J.C. Adams, The evolution of extracellular matrix, Mol. Biol. Cell 21 (2010) 4300–4305, doi:10.1091/mbc.e10-03-0251.
[7] D.A. Lauffenburger, A.F. Horwitz, Cell migration: a physically integrated molecular process, Cell 84 (1996) 359–369, doi:10.1016/S0092-8674(00)81280-5.
[8] H. Kitano, Systems biology: a brief overview, Science 295 (2002) 1662–1664, doi:10.1126/science.1069492.
[9] M.H. Zaman, L.M. Trapani, A.L. Sieminski, D. MacKellar, H. Gong, R.D. Kamm, A. Wells, D.A. Lauffenburger, P. Matsudaira, Migration of tumor cells in 3D matrices is governed by matrix stiffness along with cell-matrix adhesion and proteolysis, Proc. Natl. Acad. Sci. USA 103 (2006) 10889–10894, doi:10.1073/pnas.0604460103.
[10] A.J. Engler, S. Sen, H.L. Sweeney, D.E. Discher, Matrix elasticity directs stem cell lineage specification, Cell 126 (2006) 677–689, doi:10.1016/j.cell.2006.06.044.
[11] S. Suresh, Biomechanics and biophysics of cancer cells, Acta Biomater. 3 (2007) 413–438, doi:10.1016/j.actbio.2007.04.002.
[12] A. Saraswathibhatla, D. Indana, O. Chaudhuri, Cell–extracellular matrix mechanotransduction in 3D, Nat. Rev. Mol. Cell Biol. 24 (2023) 495–516, doi:10.1038/s41580-023-00583-1.
[13] O. Chaudhuri, J. Cooper-White, P.A. Janmey, D.J. Mooney, V.B. Shenoy, Effects of extracellular matrix viscoelasticity on cellular behaviour, Nature 584 (2020) 535–546, doi:10.1038/s41586-020-2612-2.
[14] K.M. Yamada, A.D. Doyle, J. Lu, Cell–3D matrix interactions: recent advances and opportunities, Trends Cell Biol 32 (2022) 883–895, doi:10.1016/j.tcb.2022.03.002.
[15] A.D. Doyle, N. Carvajal, A. Jin, K. Matsumoto, K.M. Yamada, Local 3D matrix microenvironment regulates cell migration through spatiotemporal dynamics of contractility-dependent adhesions, Nat. Commun. 6 (2015) 8720, doi:10.1038/ncomms9720.
[16] M.D. Davidson, K.H. Song, M.-H- Lee, J. Llewellyn, Y. Du, B.M. Baker, R.G. Wells, J.A. Burdick, Engineered fibrous networks to investigate the influence of fiber mechanics on myofibroblast differentiation, ACS Biomater. Sci. Eng. 5 (2019) 3899–3908, doi:10.1021/acsbiomaterials.8b01276.
[17] K. Wolf, M.T. Lindert, M. Krause, S. Alexander, J. Te Riet, A.L. Willis, R.M. Hoffman, C.G. Figdor, S.J. Weiss, P. Friedl, Physical limits of cell migration: control by ECM space and nuclear deformation and tuning by proteolysis and traction force, J. Cell Biol. 201 (2013) 1069–1084, doi:10.1083/jcb.201210152.
[18] T. Harada, J. Swift, J. Irianto, J.-W. Shin, K.R. Spinler, A. Athirasala, R. Diegmiller, P.C.D.P. Dingal, I.L. Ivanovska, D.E. Discher, Nuclear lamin stiffness is a barrier to 3D migration, but softness can limit survival, J. Cell Biol. 204 (2014) 669–682, doi:10.1083/jcb.201308029.
[19] B. Trappmann, B.M. Baker, W.J. Polacheck, C.K. Choi, J.A. Burdick, C.S. Chen, Matrix degradability controls multicellularity of 3D cell migration, Nat. Commun. 8 (2017) 371, doi:10.1038/s41467-017-00418-6.
[20] L. Laforgue, A. Fertin, Y. Usson, C. Verdier, V.M. Laurent, Efficient deformation mechanisms enable invasive cancer cells to migrate faster in 3D collagen networks, Sci. Rep. 12 (2022) 7867, doi:10.1038/s41598-022-11581-2.
[21] J. Solon, I. Levental, K. Sengupta, P.C. Georges, P.A. Janmey, Fibroblast adaptation and stiffness matching to soft elastic substrates, Biophys. J. 93 (2007) 4453–4461, doi:10.1529/biophysj.106.101386.
[22] M. Reimer, S. Petrova Zustiak, S. Sheth, J. Martin Schober, Intrinsic response towards physiologic stiffness is cell-type dependent, Cell Biochem. Biophys. 76 (2018) 197–208, doi:10.1007/s12013-017-0834-1.
[23] R.W. Tilghman, C.R. Cowan, J.D. Mih, Y. Koryakina, D. Gioeli, J.K. Slack-Davis, B.R. Blackman, D.J. Tschumperlin, J.T. Parsons, Matrix rigidity regulates cancer cell growth and cellular phenotype, PLoS ONE 5 (2010) e12905, doi:10.1371/journal.pone.0012905.
[24] B. Alberts, A. Johnson, J. Lewis, M. Raff, K. Roberts, P. Walter, Molecular Biology of the Cell, sixth ed., 2007 Garland Science, New York.
[25] D.T. Butcher, T. Alliston, V.M. Weaver, A tense situation: forcing tumour progression, Nat. Rev. Cancer 9 (2009) 108–122, doi:10.1038/nrc2544.
[26] M.S. Hall, F. Alisafaei, E. Ban, X. Feng, C.-Y. Hui, V.B. Shenoy, M. Wu, Fibrous nonlinear elasticity enables positive mechanical feedback between cells and ECMs, Proc. Natl. Acad. Sci. USA 113 (2016) 14043–14048, doi:10.1073/pnas.1613058113.
[27] P. Lu, V.M. Weaver, Z. Werb, The extracellular matrix: a dynamic niche in cancer progression, J. Cell Biol. 196 (2012) 395–406, doi:10.1083/jcb.201102147.
[28] B.A. Morris, B. Burkel, S.M. Ponik, J. Fan, J.S. Condeelis, J.A. Aguirre-Ghiso, J. Castracane, J.M. Denu, P.J. Keely, Collagen matrix density drives the metabolic shift in breast cancer cells, EBioMedicine 13 (2016) 146–156, doi:10.1016/j.ebiom.2016.10.012.
[29] J. Sapudom, T. Pompe, Biomimetic tumor microenvironments based on collagen matrices, Biomater. Sci. 6 (2018) 2009–2024, doi:10.1039/C8BM00303C.
[30] U.S. Schwarz, I.B. Bischofs, Physical determinants of cell organization in soft media, Med. Eng. Phys. 27 (2005) 763–772, doi:10.1016/j.medengphy.2005.04.007.
[31] M. Dembo, Y.L. Wang, Stresses at the cell-to-substrate interface during locomotion of fibroblasts, Biophys. J. 76 (1999) 2307–2316, doi:10.1016/S0006-3495(99)77386-8.
[32] J.P. Butler, I.M. Tolic-Nørrelykke, B. Fabry, J.J. Fredberg, Traction fields, moments, and strain energy that cells exert on their surroundings, Am. J. Physiol. Cell Physiol. 282 (2002) 595–605, doi:10.1152/ajpcell.00270.2001.
[33] B. Sabass, M.L. Gardel, C.M. Waterman, U.S. Schwarz, High resolution traction force microscopy based on experimental and computational advances, Biophys. J. 94 (2008) 207–220, doi:10.1529/biophysj.107.113670.
[34] D. Ambrosi, A. Duperray, V. Peschetola, C. Verdier, Traction patterns of tumor cells, J. Math. Biol. (2009) 163–181, doi:10.1007/s00285-008-0167-1.
[35] J. Steinwachs, C. Metzner, K. Skodzek, N. Lang, I. Thievessen, C. Mark, S. Münster, K.E. Aifantis, B. Fabry, Three-dimensional force microscopy of cells in biopolymer networks, Nat. Methods 13 (2016) 171–176, doi:10.1038/nmeth.3685.

[36] A. Jorge-Peñas, H. Bové, K. Sanen, M.M. Vaeyens, C. Steuwe, M. Roeffaers, M. Ameloot, H. Van Oosterwyck, 3D full-field quantification of cell-induced large deformations in fibrillar biomaterials by combining non-rigid image registration with label-free second harmonic generation, Biomaterials 136 (2017) 86–97, doi:10.1016/j.biomaterials.2017.05.015.
[37] M.M. Vaeyens, A. Jorge-Peñas, J. Barrasa-Fano, C. Steuwe, T. Heck, P. Carmeliet, M. Roeffaers, H. Van Oosterwyck, Matrix deformations around angiogenic sprouts correlate to sprout dynamics and suggest pulling activity, Angiogenesis 23 (2020) 315–324, doi:10.1007/s10456-020-09708-y.
[38] V. Peschetola, V.M. Laurent, A. Duperray, R. Michel, D. Ambrosi, L. Preziosi, C. Verdier, Time-dependent traction force microscopy for cancer cells as a measure of invasiveness, Cytoskeleton 70 (2013) 201–214, doi:10.1002/cm.21100.
[39] I. Rabinovitz, I.K. Gipson, A.M. Mercurio, Traction Forces Mediated by $\alpha 6\beta 4$ integrin: implications for basement membrane organization and tumor invasion, Mol. Biol. Cell. 12 (2001) 4030–4043, doi:10.1091/mbc.12.12.4030.
[40] J. Figueiredo, R.M. Ferreira, H. Xu, M. Gonçalves, A. Barros-Carvalho, J. Cravo, A.F. Maia, P. Carneiro, C. Figueiredo, M.L. Smith, D. Stamenović, E. Morais-de-Sá, R. Seruca, Integrin $\beta 1$ orchestrates the abnormal cell-matrix attachment and invasive behaviour of E-cadherin dysfunctional cells, Gastric Cancer 25 (2022) 124–137, doi:10.1007/s10120-021-01239-9.
[41] C.M. Kraning-Rush, S.P. Carey, J.P. Califano, C.A. Reinhart-King, Quantifying traction stresses in adherent cells, Methods Cell Biol. 10 (2012) 139–178, doi:10.1016/B978-0-12-388403-9.00006-0.
[42] X. Tang, A. Tofangchi, S.V. Anand, T.A. Saif, A novel cell traction force microscopy to study multi-cellular system, PLoS Comput. Biol. 10 (2014) e1003631, doi:10.1371/journal.pcbi.1003631.
[43] D. Li, H. Colin-York, L. Barbieri, Y. Javanmardi, Y. Guo, K. Korobchevskaya, E. Moeendarbary, D. Li, M. Fritzsche, Astigmatic traction force microscopy (aTFM), Nat. Commun., 12 (2021) 2168. https://doi.org/10.1038/s41467-021-22376-w
[44] J.R. Tse, A.J. Engler, Preparation of hydrogel substrates with tunable mechanical properties, Curr. Protoc. Cell Biol. 47 (2010) 10–16, doi:10.1002/0471143030.cb1016s47.
[45] X. Li, Q. Sun, Q. Li, N. Kawazoe, G. Chen, Functional hydrogels with tunable structures and properties for tissue engineering applications, Front. Chem. 6 (2018) 499, doi:10.3389/fchem.2018.00499.
[46] W.G. Herrick, T.V. Nguyen, M. Sleiman, S. McRae, T.S. Emrick, S.R. Peyton, PEG-phosphorylcholine hydrogels as tunable and versatile platforms for mechanobiology, Biomacromolecules 14 (2013) 2294–2304, doi:10.1021/bm400418g.
[47] M. Shayan, M.S. Huang, R. Navarro, G. Chiang, C. Hu, B.P. Oropeza, P.K. Johansson, R.A. Suhar, A.A. Foster, B.L. LeSavage, M. Zamani, A. Enejder, J.G. Roth, S.C. Heilshorn, N.F. Huang, Elastin-like protein hydrogels with controllable stress relaxation rate and stiffness modulate endothelial cell function, J. Biomed. Mater. Res. A. 111 (2023) 896–909, doi:10.1002/jbm.a.37520.
[48] Z. Liu, J. Fu, H. Yuan, B. Ma, Z. Cao, Y. Chen, X. Xing, X. Niu, N. Li, H. Wang, H. An, Polyisocyanide hydrogels with tunable nonlinear elasticity mediate liver carcinoma cell functional response, Acta Biomater. 148 (2022) 152–162, doi:10.1016/j.actbio.2022.06.022.
[49] E. Cambria, M.F. Coughlin, M.A. Floryan, G.S. Offeddu, S.E. Shelton, R.D. Kamm, Linking cell mechanical memory and cancer metastasis, Nat. Rev. Cancer 24 (2024) 216–228, doi:10.1038/s41568-023-00656-5.
[50] C. Fan, D.A. Wang, Effects of permeability and living space on cell fate and neotissue development in hydrogel-based scaffolds: a study with cartilaginous model, Macromol. Biosci. 15 (2015) 535–545, doi:10.1002/mabi.201400453.
[51] W. Leong, A. Kremer, D.A. Wang, Development of size-customized hepatocarcinoma spheroids as a potential drug testing platform using a sacrificial gelatin microsphere system, Mater. Sci. Eng. C. 63 (2016) 644–649, doi:10.1016/j.msec.2016.03.046.
[52] X. Li, Y. Chen, N. Kawazoe, G. Chen, Influence of microporous gelatin hydrogels on chondrocyte functions, J. Mater. Chem. B. 5 (2017) 5753–5762, doi:10.1039/C7TB01350G.
[53] C.K. Arakawa, B.A. Badeau, Y. Zheng, C.A. DeForest, Multicellular vascularized engineered tissues through user-programmable biomaterial photodegradation, Adv. Mat. 29 (2017), doi:10.1002/adma.201703156.
[54] B. Zhang, M. Montgomery, M.D. Chamberlain, S. Ogawa, A. Korolj, A. Pahnke, L.A. Wells, S. Massé, J. Kim, L. Reis, A. Momen, S.S. Nunes, A.R. Wheeler, K. Nanthakumar, G. Keller, M.V. Sefton, M. Radisic, Biodegradable scaffold with built-in vasculature for organ-on-a-chip engineering and direct surgical anastomosis, Nat. Mater. 15 (2016) 669–678, doi:10.1038/nmat4570.
[55] L.M. Jawerth, S. Münster, D.A. Vader, B. Fabry, D.A. Weitz, A blind spot in confocal reflection microscopy: the dependence of fiber brightness on fiber orientation in imaging biopolymer networks, Biophys. J. 98 (2010) L1–L3, doi:10.1016/j.bpj.2009.09.065.
[56] C.A. Garrido, D.S. Garske, M. Thiele, S. Amini, S. Real, G.N. Duda, K. Schmidt-Bleek, A. Cipitria, Hydrogels with stiffness-degradation spatial patterns control anisotropic 3D cell response, Biomater. Adv. 151 (2023) 213423, doi:10.1016/j.bioadv.2023.213423.
[57] H. Wang, A. Abhilash, C.S. Chen, R.G. Wells, V.B. Shenoy, Long-range force transmission in fibrous matrices enabled by tension-driven alignment of fibers, Biophys. J. 107 (2014) 2592–2603, doi:10.1016/j.bpj.2014.09.044.
[58] Y. Du, S.C. Herath, Q.G. Wang, H. Asada, P.C. Chen, Determination of Green's function for three-dimensional traction force reconstruction based on geometry and boundary conditions of cell culture matrices, Acta Biomater. 67 (2018) 215–228, doi:10.1016/j.actbio.2017.12.002.
[59] H.J. Bowers, E.E. Fannin, A. Thomas, J.A. Weis, Characterization of multicellular breast tumor spheroids using image data-driven biophysical mathematical modeling, Sci. Rep. 10 (2020) 11583, doi:10.1038/s41598-020-68324-4.
[60] T. Hildebrand, P. Rüegsegger, A new method for the model-independent assessment of thickness in three-dimensional images, J. Micros. 185 (1997) 67–75, doi:10.1046/j.1365-2818.1997.1340694.x.
[61] J. Barrasa-Fano, A. Shapeti, A. Jorge-Peñas, M. Barzegari, J.A. Sanz-Herrera, H. Van Oosterwyck, TFMLAB: a MATLAB toolbox for 4D traction force Microscopy, SoftwareX 15 (2021) 100723, doi:10.1016/j.softx.2021.100723.
[62] A. Jorge-Peñas, A. Izquierdo-Alvarez, R. Aguilar-Cuenca, M. Vicente-Manzanares, J.M. Garcia-Aznar, H. Van Oosterwyck, E.M. de-Juan-Pardo, C. Ortiz-de-Solozano, A. Munoz-Barrutia, Free form deformation–based image registration improves accuracy of traction force microscopy, PLoS ONE 10 (2015) e0144184, doi:10.1371/journal.pone.0144184.
[63] J.A. Sanz-Herrera, J. Barrasa-Fano, M. Cóndor, H. Van Oosterwyck, Inverse method based on 3D nonlinear physically constrained minimisation in the framework of traction force microscopy, Soft Matter 17 (2021) 10210–10222, doi:10.1039/D0SM00789G.
[64] A. Apolinar-Fernández, J. Barrasa-Fano, M. Cóndor, H. Van Oosterwyck, J.A. Sanz-Herrera, Traction force reconstruction assessment on real three-dimensional matrices and cellular morphologies, Int. J. Eng. Sci. 186 (2023) 103828, doi:10.1101/2022.11.16.516745.
[65] A.A. Solbu, D. Caballero, S. Damigos, S.C. Kundu, R.L. Reis, Ø. Halaas, A.S. Chahal, B.L. Strand, Assessing cell migration in hydrogels: an overview of relevant materials and methods, Mater. Today Bio 18 (2023) 100537, doi:10.1016/j.mtbio.2022.100537.
[66] J. Hazur, N. Endrizzi, D.W. Schubert, A.R. Boccaccini, B. Fabry, Stress relaxation amplitude of hydrogels determines migration, proliferation, and morphology of cells in 3-D culture, Biomater. Sci. 10 (2022) 270–280, doi:10.1039/D1BM01089A.
[67] T.R. Cox, J.T. Erler, Remodeling and homeostasis of the extracellular matrix: implications for fibrotic diseases and cancer, Dis. Model Mech. 4 (2011) 165–178, doi:10.1242/dmm.004077.
[68] M. Urbanczyk, S.L. Layland, K. Schenke-Layland, The role of extracellular matrix in biomechanics and its impact on bioengineering of cells and 3D tissues, Matrix Biol 85 (2020) 1–14, doi:10.1016/j.matbio.2019.11.005.
[69] D. Velegol, F. Lanni, Cell traction forces on soft biomaterials. I. Microrheology of type I collagen gels, Biophys. J. 81 (2001) 1786–1792, doi:10.1016/S0006-3495(01)75829-8.
[70] Y. Shinsato, A.D. Doyle, W. Li, K.M. Yamada, Direct comparison of five different 3D extracellular matrix model systems for characterization of cancer cell migration, Cancer Rep. 3 (2020) e1257, doi:10.1002/cnr2.1257.
[71] E.E. Antoine, P.P. Vlachos, M.N. Rylander, Review of collagen I hydrogels for bioengineered tissue microenvironments: characterization of mechanics, structure, and transport, Tissue Eng. Part B 20 (2014) 683–696, doi:10.1089/ten.TEB.2014.0086.
[72] S.P. Reese, N. Farhang, R. Poulson, G. Parkman, J.A. Weiss, Nanoscale imaging of collagen gels with focused ion beam milling and scanning electron microscopy, Biophys. J. 111 (2016) 1797–1804, doi:10.1016/j.bpj.2016.08.039.
[73] L.J. Gibson, Biomechanics of cellular solids, J. Biomech. 38 (2005) 377–399, doi:10.1016/j.jbiomech.2004.09.027.
[74] A. Hayn, T. Fischer, C.T. Mierke, Inhomogeneities in 3D collagen matrices impact matrix mechanics and cancer cell migration, Front. Cell Dev. Biol. 8 (2020) 593879, doi:10.3389/fcell.2020.593879.
[75] J.A. Van Der Rijt, K.O. Van Der Werf, M.L. Bennink, P.J. Dijkstra, J. Feijen, Micromechanical testing of individual collagen fibrils, Macromol. Biosci. 6 (2006) 697–702, doi:10.1002/mabi.200600063.
[76] M.P. Wenger, L. Bozec, M.A. Horton, P. Mesquida, Mechanical properties of collagen fibrils, Biophys. J. 93 (2007) 1255–1263, doi:10.1529/biophysj.106.103192.
[77] M. Tamayo-Angorrilla, J.L. de Andrés, G. Jiménez, J.A. Marchal, The biomimetic extracellular matrix: a therapeutic tool for breast cancer research, Transl. Res. 247 (2022) 117–136, doi:10.1016/j.trsl.2021.11.008.
[78] Z.N. Demou, M. Awad, T. McKee, J.Y. Perentes, X. Wang, L.L. Munn, R.K. Jain, Y. Boucher, Lack of telopeptides in fibrillar collagen I promotes the invasion of a metastatic breast tumor cell line, Cancer Res 65 (2005) 5674–5682, doi:10.1158/0008-5472.CAN-04-1682.
[79] M. Cavo, M. Caria, I. Pulsoni, F. Beltrame, M. Fato, S. Scaglione, A new cell-laden 3D Alginate-Matrigel hydrogel resembles human breast cancer cell malignant morphology, spread and invasion capability observed "in vivo", Sci. Rep. 8 (2018) 5333, doi:10.1038/s41598-018-23250-4.
[80] T.M. Koch, S. Münster, N. Bonakdar, J.P. Butler, B. Fabry, 3D traction forces in cancer cell invasion, PLoS ONE 7 (2012) e33476, doi:10.1371/journal.pone.0033476.
[81] E.L. Baker, M.H. Zaman, The biomechanical integrin, J. Biomech. 43 (2010) 38–44, doi:10.1016/j.jbiomech.2009.09.007.
[82] T. Razafiarison, C.N. Holenstein, T. Stauber, M. Jovic, E. Vertudes, M. Loparic, M. Kawecki, L. Bernard, U. Silvan, J.G. Snedeker, Biomaterial surface energy-driven ligand assembly strongly regulates stem cell mechanosensitivity and fate on very soft substrates, Proc. Natl. Acad. Sci. 115 (2018) 4631–4636, doi:10.1073/pnas.1704543115.
[83] J.P. Califano, C.A. Reinhart-King, Substrate stiffness and cell area predict cellular traction stresses in single cells and cells in contact, Cell. Mol. Bioeng. 3 (2010) 68–75, doi:10.1007/s12195-010-0102-6.
[84] C.A. Reinhart-King, M. Dembo, D.A. Hammer, The dynamics and mechanics of endothelial cell spreading, Biophys. J. 89 (2005) 676–689, doi:10.1529/biophysj.104.054320.

[85] M. Ghibaudo, A. Saez, B. Ladoux, Traction forces and rigidity sensing regulate cell functions, Soft Matter 4 (2008) 1836–1843, doi:10.1039/B804103B.
[86] C.M. Kraning-Rush, J.P. Califano, C.A. Reinhart-King, Cellular traction stresses increase with increasing metastatic potential, PLoS ONE 7 (2012) e32572, doi:10.1371/journal.pone.0032572.
[87] P.A. Janmey, D.A. Fletcher, C.A. Reinhart-King, Stiffness sensing by cells, Physiol. Rev. 100 (2020) 695–724, doi:10.1152/physrev.00013.2019.
[88] S. Lin, M.C. Lampi, C.A. Reinhart-King, G. Tsui, J. Wang, C.A. Nelson, L. Gu, Eigenstrain as a mechanical set-point of cells, Biomech. Model. Mechanobiol. 17 (2018) 951–959, doi:10.1007/s10237-018-1004-0.
[89] A.D. Doyle, S.S. Nazari, K.M. Yamada, K. M., Cell–extracellular matrix dynamics, Phys. Biol. 19 (2022) 021002, doi:10.1088/1478-3975/ac4390.
[90] A.D. Doyle, D.J. Sykora, G.G. Pacheco, M.L. Kutys, K.M. Yamada, 3D mesenchymal cell migration is driven by anterior cellular contraction that generates an extracellular matrix prestrain, Dev. Cell 56 (2021) 826–841, doi:10.1016/j.devcel.2021.02.017.
[91] M. Anguiano, X. Morales, C. Castilla, A.R. Pena, C. Ederra, M. Martínez, M. Ariz, M. Esparza, H. Amaveda, M. Mora, N. Movilla, J.M. García-Aznar, I. Cortés-Domínguez, The use of mixed collagen-Matrigel matrices of increasing complexity recapitulates the biphasic role of cell adhesion in cancer cell migration: ECM sensing, remodeling and forces at the leading edge of cancer invasion, PLoS ONE 15 (2020) e0220019, doi:10.1371/journal.pone.0220019.
[92] A. Pathak, V.S. Deshpande, A.G. Evans, R.M. McMeeking, Simulations of cell behavior on substrates of variegated stiffness and architecture, in: G. Holzapfel, E. Kuhl (Eds.), Computer Models in Biomechanics, Springer Netherland, Dordrecht, 2013, doi:10.1007/978-94-007-5464-5_3.
[93] D. Lu, Z. Zeng, Z. Geng, C. Guo, D. Pei, J. Zhang, S. Yu, Macroporous methacrylated hyaluronic acid hydrogel with different pore sizes for in vitro and in vivo evaluation of vascularization, Biomed. Mater. 17 (2022) 025006, doi:10.1088/1748-605X/ac494b.
[94] J.R. Lange, B. Fabry, Cell and tissue mechanics in cell migration, Exp. Cell Res. 319 (2013) 2418–2423, doi:10.1016/j.yexcr.2013.04.023.
[95] K. Wolf, S. Alexander, V. Schacht, L.M. Coussens, U.H. von Andrian, J. van Rheenen, E. Deryugina, P. Friedl, Collagen-based cell migration models in vitro and in vivo, Semin. Cell Dev. Biol. 20 (2009) 931–941, doi:10.1016/j.semcdb.2009.08.005.
[96] B. Yi, Q. Xu, W. Liu, An overview of substrate stiffness guided cellular response and its applications in tissue regeneration, Bioact. Mater. 15 (2021) 82–102, doi:10.1016/j.bioactmat.2021.12.005.
[97] Y.C. Yeh, J.Y. Ling, W.C. Chen, H.H. Lin, M.J. Tang, Mechanotransduction of matrix stiffness in regulation of focal adhesion size and number: reciprocal regulation of caveolin-1 and β1 integrin, Sci. Rep. 7 (2017) 15008, doi:10.1038/s41598-017-14932-6.
[98] G.L. Lin, D.M. Cohen, R.A. Desai, M.T. Breckenridge, L. Gao, M.J. Humphries, C.S. Chen, Activation of beta 1 but not beta 3 integrin increases cell traction forces, FEBS Lett. 587 (2013) 763–769 http://doi.org/10.1016/j.febslet.2013.01.068.